



PONTIFICIA UNIVERSIDAD CATOLICA DE CHILE  
SCHOOL OF ENGINEERING

# **EXPERIMENTAL AND SIMULATION STUDY OF ELECTRON AND PHONON PROPERTIES IN CRYSTALLINE MATERIALS**

**JORGE OSVALDO MORALES FERREIRO**

Members of the Committee:

**DIEGO CELENTANO**

**TENGFELUO**

**DAVID GO**

**YANLIANG ZHANG**

**DONOVAN DÍAZ DROGETT**

**MAGDALENA WALCZAK**

Thesis submitted to the Office of Graduate Studies in partial fulfillment of the requirements for the Degree of Master of Science in Engineering and Doctor in Engineering Sciences

Santiago de Chile, September, 2018

EXPERIMENTAL AND SIMULATION STUDY OF  
ELECTRON AND PHONON PROPERTIES IN CRYSTALLINE  
MATERIALS

A Dissertation

Submitted to the Graduate School  
of the University of Notre Dame  
in Partial Fulfillment of the Requirements  
for the Degree of

Doctor of Philosophy

by

Jorge Morales Ferreiro

Graduate Program in Aerospace and Mechanical Engineering

Notre Dame, Indiana

September 2018

© Copyright 2018

Jorge O. Morales

All Rights Reserved

# EXPERIMENTAL AND SIMULATION STUDY OF ELECTRON AND PHONON PROPERTIES IN CRYSTALLINE MATERIALS

Abstract

By

Jorge O. Morales

The continuous increase in demand of electrical energy has become a major concern for many countries. The world has seen a constant search for new alternative energy resources mainly focusing on resources that are environmentally friendly. One technology that goes in that direction is thermoelectrics.

Thermoelectrics can directly convert a temperature difference into electrical current or vice versa. The mechanism behind such devices is the thermoelectric effect, which is referred to as the Seebeck or Peltier effect. A good thermoelectric material needs the simultaneous optimization of three key properties to reach a high efficiency, which can usually be characterized by the figure of merit ( $ZT$ ): high Seebeck coefficient, high electrical conductivity, and low thermal conductivity. However, maximizing one property while minimizing the other is a difficult task, because materials tend either to conduct both electricity and heat well, or both poorly.

The study of thermal properties plays important roles in many applications as thermoelectricity and the thermal management of electronic devices. While phonons dominate the thermal transport in crystalline semiconductors, electrons are the major thermal and chargecarriers in metals. A deeply understanding of the transport properties of electrons and phonons will allow improvement in thermal management and better nanoscale materials design.

The overarching goal of this thesis is to study the electron and phonon transport properties in both bulk and two-dimensional crystalline materials, which could provide important insights to the electronic and thermal transport physics in these materials. The aim of this thesis is to use both simulation and experimental tools to study the electron and phonon transport properties of crystalline materials such as SnSe, SnS, GeS, GeSe, SnS<sub>2</sub>, SnSe<sub>2</sub>, and NbSe<sub>2</sub>. Regarding the experimental study, we used the structural and morphological characterization of bulk SnSe, to determine its microstructure and crystallinity. In addition, thermoelectric properties were measured, where the  $ZT$  reaches a value of 0.11 at 772 K. Moreover, we studied electron-phonon interaction from first-principles calculations using density functional theory and Boltzmann transport equation. The intrinsic electrical and thermal properties of monolayer SnSe, SnS, GeS, GeSe, SnS<sub>2</sub>, and SnSe<sub>2</sub>, at different doping levels are calculated, helping evaluate their potential as thermoelectric materials. SnSe was found with the largest  $ZT$ , which was related to the low lattice thermal conductivity of this material. Regarding phonon transport, we applied first-principles lattice dynamics and semi-empirical Boltzmann transport to study the phonon properties and lattice thermal conductivity of NbSe<sub>2</sub>, and compare the results obtained from an experimental approach. Our estimation of thermal conductivity of 13.5 W/mK, are in good agreement with the in-plane thermal conductivity obtained from experiments, where the thermal conductivity is measured to be  $14 \pm 5$  W/mK at room temperature.

Dedicated to my parents, María Eugenia and Yayo, my sisters Catalina and Belén, and my loved  
sons Matías and Tomás, whose unconditional love was a source of effort, encouragement and  
inspiration

## CONTENTS

CHAPTER 1: INTRODUCCION.....	1
1.1. Motivation.....	1
1.2. Theories: a basic approach.....	3
1.2.1. Thermoelectricity Fundamentals .....	3
1.2.2. Density Functional Theory .....	7
1.2.3. Boltzmann Transport Theory.....	10
1.2.4. X-ray Diffraction Technique (XRD) .....	11
1.2.5. Scanning Electronic Microscope Technique (SEM).....	12
1.2.6. Raman Spectroscopy.....	13
1.3. Hypothesis of this research .....	14
1.4. Research challenges and Objectives .....	14
1.4.1. Effect of the Annealing of the Power Factor of Un-Doped Cold Pressed SnSe.....	14
1.4.2. First-Principles Calculations of Thermoelectric Properties of IV-VI Chalcogenides 2D Materials .....	14
1.4.3. In-Plane Thermal Conductivity of the Niobium Diselenide from Temperature-Dependent Raman Spectroscopy .....	15
1.5. Methodology .....	15
1.6. Principal results and conclusions .....	16
1.7. Organization of the Thesis .....	17
CHAPTER 2: EFFECT OF THE ANNEALING ON THE POWER FACTOR OF UN- DOPED COLD PRESSED SnSe .....	18
2.1. Background.....	18
2.2. Experimental Details.....	19
2.2.1. Sample preparation .....	19
2.2.2. Sample Characterization .....	20
2.2.3. X-ray Diffraction (XRD) .....	20
2.2.4. Scanning Electron Microscopy (SEM) .....	21
2.3. Measurement of Transport Properties.....	21
2.4. Crystallographic Features .....	22
2.5. Microstructure.....	23
2.6. Thermoelectric Properties.....	25
2.6.1. Seebeck Coefficient .....	25

2.6.2. Electrical Conductivity .....	26
2.6.3. Power Factor .....	27
2.6.4. Thermal Conductivity .....	29
2.6.5. Figure of Merit .....	33
CHAPTER 3: FIRST-PRINCIPLES CALCULATIONS OF THERMOELECTRIC PROPERTIES OF IV-VI CHACOGENIDES 2D MATERIALS .....	34
3.1 Background .....	34
3.2 Computational details .....	35
3.3 Band Structures .....	40
3.4 Thermoelectric properties .....	42
CHAPTER 4: IN-PLANE THERMAL CONDUCTIVITY OF THE NIOBIUM DISELENIDE FROM TEMPERATURE-DEPENDENT RAMAN SPECTROSCOPY.....	48
4.1 Background .....	48
4.2 Results and discussion .....	49
CHAPTER 5: CONCLUSIONS AND FUTURE WORK.....	56
5.1. Conclusions.....	56
5.2. Future Work .....	57

## LIST OF FIGURES

Figure 1.1. Schematics of a TE cooler, a thermoelectric generator and a TE device based on <i>n</i> - and <i>p</i> -type semiconductors. (a) Scheme of a TE cooler (TEC). (b) Scheme of a TE generator (TEG). The arrows in the segments illustrate the electric current flow (blue: low temperature, red: high temperature) <sup>50</sup> .....	4
Figure 1.2. Maximizing the efficiency ZT of a thermoelectric material. The three parameters: thermal conductivity, electrical conductivity, and Seebeck coefficient are involved. Good thermoelectric materials are typically heavily doped semiconductors with a carrier concentration between $10^{19}$ and $10^{21}$ charge carriers per $\text{cm}^3$ .....	7
Figure 1.3. Diagram of Bragg's law <sup>58</sup> .....	12
Figure 2.1. Illustration of orthorhombic crystal structure of SnSe .....	18
Figure 2.2. Flow of samples' preparation and thermoelectric properties' measurement.....	20
Figure 2.3. (a) Sample before annealing, (b) sample after annealing, and (c) reference XRD pattern of SnSe <sup>62</sup> .....	23
Figure 2.4. SEM images acquired from an un-doped SnSe tablet. (a) center and (b) edge of the sample before annealing. (c) center and (d) edge of the sample after annealing .....	24
Figure 2.5. (a) Seebeck coefficient ( <i>S</i> ) values, (b) electrical conductivity ( $\sigma$ ), and (c) power factor (PF) as a function of temperature of un-doped polycrystalline SnSe .....	29
Figure 2.6. (a) Thermal diffusivity ( <i>h</i> ), (b) lattice ( <i>kl</i> ), electronic ( <i>ke</i> ), and thermal ( <i>k</i> ) conductivity of un-doped SnSe polycrystalline, and (c) thermal conductivity of this work compared with references .....	32
Figure 2.7. $\log kl - \log T$ of un-doped polycrystalline SnSe sample .....	32
Figure 2.8. Figure of merit (ZT) as a function of temperature of un-doped polycrystalline SnSe	33
Figure 3.1. Schematic of the flow chart for TE properties and lattice thermal conductivity calculations .....	37
Figure 3.2. Crystal structures of (a) orthorhombic and (b) hexagonal materials .....	39
Figure 3.3. Band structures of TE materials (top row) without SOC and (bottom row) with SOC .....	41
Figure 3.4. Seebeck coefficient as a function of temperature (a-c) without SOC and (d-f) with SOC at different doping levels.....	43
Figure 3.5. TE properties as a function of temperature without SOC at different doping levels .	45
Figure 3.6. Lattice thermal conductivity of 2D TE materials as a function of temperature .....	46
Figure 4.1. Crystal structures of bulk NbSe <sub>2</sub> . For 2D NbSe <sub>2</sub> , we will only simulate one single molecular layer.....	49
Figure 4.2. (a) Lattice thermal conductivity and (b) cumulative thermal conductivity of NbSe <sub>2</sub> .	51

Figure 4.3. Phonon dispersion of NbSe <sub>2</sub> .....	53
Figure 4.4. (a) Phonon group velocity, (b) relaxation times, (c) scattering phase space, and (d) Gruneisen parameter of NbSe <sub>2</sub> .....	54

## LIST OF TABLES

Table 1. Literature and our optimized lattice parameters for all the 2D materials studied.....	36
Table 2. Comparison of band gap energies (eV) with and without SOC for the 2D semiconductors. ....	41

## ACKNOWLEDGMENTS

I have spent almost five years as a graduate student between Pontificia Universidad Católica de Chile and University of Notre Dame. The experience has been enjoyable and rewarding, and not less complex and challenging by many passages. Reaching this final step would not have been possible without the help, support and guidance of my mentors, teachers, friends and family.

I am grateful to many people. In particular, I want to thank my advisors, Dr. Tengfei Luo, Dr. Diego Celentano and Dr. Donovan Díaz, for their unconditional and generous support, guidance and limitless patient. Without it, I would not be able to focus on the topics and when I hit obstacles. Dr. Luo, Dr. Celentano and Dr. Díaz are so passionate about research. They have great vision and deep understanding of our research field, but also have the flexibility and an open mind to grant me the freedom to explore my own interests and provide guidance when I get lost in uncharted land. I have learnt so much from them about in-depth knowledge, research methods, and ethics; without doubt they are the role model for me and have set up very high standards that I will try hard in my research and life. I would also like to express my sincere gratitude to my PhD committee members, Dr. Griselda García, Dr. Julio Vergara, Dr. Rodrigo Espinoza, Dr. David Go and Dr. Yanliang Zhang for their valuable comments, suggestions, and instructions during my PhD research. Also, I want to thank Dr. Clivia Sotomayor Torres for provide me her invaluable advice and suggestions about my present and future research, and for accepting me in her research group as a visiting student. Also, I want to thank Dr. Mihir Sen for his suggestion to come to Notre Dame, without doubt it was the right decision that changed my life.

Many thanks to the members of Molecular-level Energy and Mass Transport Laboratory and special thanks to Dr. Teng Zhang, Dr. Xufei Wu, Dr. Shirui Luo, Mr. Zeyu Liu, and Mr. Yunsong Pang, for their valuable discussions and supports. Many thanks to our collaborators, Dr. Sabyasachi Ganguli, Dr. Vikas Varshney, and Dr. Huili Grace Xin for their generous helps and useful discussions. I would like special thanks to my wonderful friends who have made my life so amazing.

Finally, I want to thank all my family, specially my parents María Eugenia and Yayo, my sisters Catalina and Belén, and my little and loved boys Matías and Tomás, for they unconditional support and love in the entire process to complete my PhD study.

At last, I want to thank to the Chilean Council for Scientific and Technological Research (CONICYT) for the support of this research.

## CHAPTER 1: INTRODUCTION

### 1.1. Motivation

The world has been in a constant search for alternative energy resources with better sustainability than the currently dominant fossil fuels. One of the technologies that has attracted attention not only in the scientific community but also in industry is the development and application of thermoelectric (TE) materials, which are capable of converting heat directly into electricity.<sup>1-3</sup> The central question in this field is how to improve the energy conversion efficiency of TE materials and devices so that they can be a competitive alternative to conventional energy conversion technologies. If this is realized, TE technologies could take more active roles in improving the overall efficiency of existing thermal energy systems, reducing reliance on fossil fuels, or in some scenario replacing fossil fuels with the aid of non-conventional renewable energy (NCRE) such as solar-thermal systems.<sup>4-7</sup>

A good TE material must exhibit a high performance usually characterized by the figure-of-merit  $ZT$  defined as:  $ZT = S^2\sigma T/k$ , where  $S$  is the Seebeck coefficient (i.e., generated voltage due to a given temperature gradient),  $\sigma$  is the electrical conductivity of the material,  $T$  is the absolute temperature in Kelvin, and  $k$  is the total thermal conductivity including contributions from both phonons and electrons. Nowadays, one of the most important challenges is finding TE materials with high values of  $ZT$ . However, due to the intrinsically inter-correlated properties ( $S$ ,  $\sigma$ , and  $k$ ) in  $ZT$ , the optimization of the efficiencies of TE materials has been challenging. Most of the TE materials have  $ZT$  less than 1 and only a few have  $ZT$  between 1 and 2.<sup>8-13</sup> Recently, record-high  $ZT$  values (maximum values measured between 700 K and 950 K) ranging from 2.2

to 2.6 for single crystals of SnSe have been reported,<sup>14,15</sup> placing TE-based devices in a competitive position to traditional mechanical energy conversion systems. However, it should be noted that the use of single crystals for industrial applications might face other difficulties due to their poor mechanical properties. With potentially better mechanical properties and lower cost, polycrystalline SnSe, both doped and un-doped, has been studied, and  $ZT$  values ranging from 0.5 to 1 have been reported.<sup>16–20</sup> However, further developments on polycrystalline SnSe to improve its  $ZT$  to be closer to that of its single crystalline counterpart is of great scientific and engineering significance. In recent years, the field has witnessed great progress in improving the  $ZT$  of different TE materials.<sup>21–25</sup> Success has mainly come from the reduction of lattice thermal conductivity by either nanostructuring conventional TE materials<sup>3,21,22</sup> or choosing new compounds with intrinsic low thermal conductivities.<sup>14,15</sup> In the meantime, improving the electrical properties (Seebeck coefficient and electrical conductivity) has also been under intensive investigation and success has been achieved through methods like resonant doping and band convergence.<sup>12,13,25–27</sup> In many of these TE materials, microstructures play pivotal roles in linking the processing and synthesis conditions with the improvement of the properties. There are a number of topical reviews that describe different mechanisms to improve these properties and thus increase the  $ZT$ .<sup>28–30</sup>

Additionally, the discovery of 2D materials, exemplified by graphene<sup>31,32</sup> and transition metal dichalcogenides (TMDC),<sup>33–37</sup> has stimulated much research interests due to their unique structural, mechanical, optical, electrical and thermal properties,<sup>1,25,38,39</sup> potential applications in photovoltaics,<sup>40</sup> transistors,<sup>41,42</sup> optoelectronics,<sup>43</sup> photodetector and molecular sensing,<sup>44</sup> and wearable heating and cooling.<sup>29,45,46</sup> Moreover, due to their intrinsic band gaps, TMDC monolayers have better potential in nanoelectronics applications compared to graphene.

Additionally, TMDC materials have relatively high electrical properties such as Seebeck coefficient and electrical conductivity compared with other 2D materials such as black phosphorene,<sup>47</sup> positioning them as good candidates for TE applications. Although a large range of thermal conductivity has been reported for TMDCs, mostly with values higher than 30 W/mK, values for suspended monolayer in the order of 15 W/mK or less have been observed recently.<sup>19,48</sup> It has been reported that the TE properties of 2D materials can also be unique because any modification to their environment or chemical functionalization, which play significant roles in thermal and electronic transport, can greatly impact their TE properties.<sup>30</sup>

## 1.2. Theories: a basic approach

In this section, a brief description of simulation and experimental theories used in this research are presented. From simulation theories, we introduce the most important concepts of Thermoelectricity fundamentals, Density Functional Theory (DFT), and Boltzmann transport theory; from experimental theory X-ray diffraction (XRD), Scanning Electronic Microscope (SEM), and Raman spectroscopy is presented.

### 1.2.1. Thermoelectricity Fundamentals

Thermoelectricity involves a fundamental interaction between the electronic and thermal properties of a material. TE materials can be used for direct heat to electricity conversion by Seebeck effect, where the temperature gradient drives the thermal diffusion of charge carriers. TE fundamentals can be explained through the movement of electrons (n) and holes (p), which act as mobile charge carriers. Those at the hot side of the material have more thermal energy than carriers at the cold side, causing a net diffusion of mobile carriers to the cold side. Since there are more mobile carriers at the cold side than the hot side, the non-homogeneous charge distribution forms an electric field, which opposes the diffusion. If the material is in an open circuit (Figure

1.1 a), equilibrium will be reached when the rate at which carriers move from the hot side to the cold side due to diffusion is balanced by the rate at which carriers move from the cold side to the hot side due to the electric field. Thus, in equilibrium an electrochemical potential difference will form in response to a temperature gradient. This electrochemical potential difference is known as the Seebeck voltage, and the amount of voltage generated per unit temperature gradient is called the Seebeck coefficient ( $S$ ). If the material is connected to a circuit (Figure 1.1 b), the electrochemical potential will drive a current, which can be used to perform electrical work, this being the basis for thermoelectric power generation.<sup>49,50</sup>

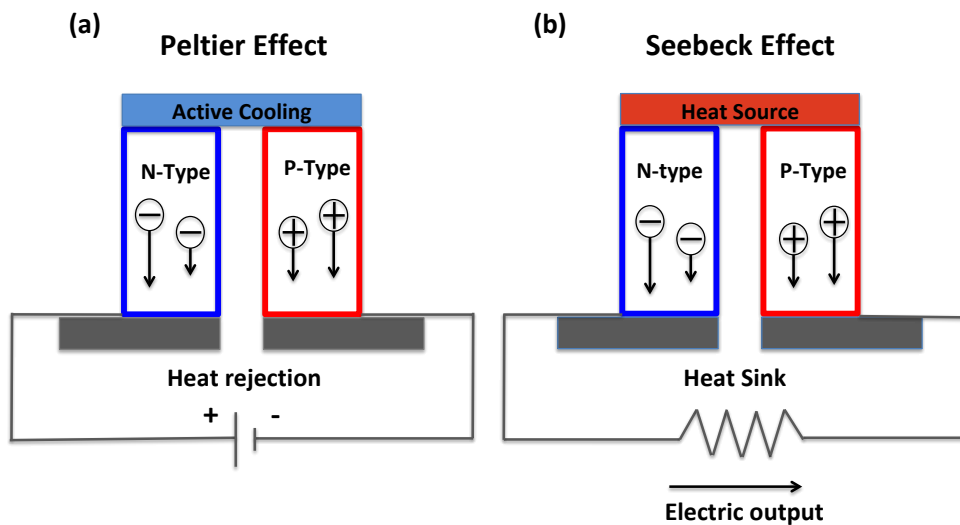


Figure 1.1. Thermoelectric generator based on  $n$ - and  $p$ -type semiconductors. (a) Scheme of TE cooler (TEC), (b) Scheme of TE generator (TEG).

Abram Fedorovich Ioffe (1950s) established the basis for the modern theory of thermoelectricity. He focused on studies of electrical and thermal transport properties of a new class of solids that he later called semiconductors.<sup>1</sup> Ioffe recognized semiconductors as potential materials with high TE efficiency conversion. Materials of interest were particularly bulk PbS,

PbTe, PbSe, ZnSb, Bi<sub>2</sub>Te<sub>3</sub>, and Sb<sub>2</sub>Te<sub>3</sub>. Sixty-four years later, those materials continue being studied. New families of TE materials have attracted most attention in the last decade. The aforementioned materials, SiGe alloy, Half-Heuslers, Chalcogenides, Perovskites, Skutterudites, Oxides and others,<sup>12,13,51,52</sup> have been proven to be promising candidates for future technological applications.

TE materials can also be used as solid-state refrigerators or heat pumps by driving a current in a circuit with two dissimilar materials. This mode exploits the Peltier effect, discovered by Jean-Charles Peltier in 1834, where heat is absorbed or rejected at the interface of two dissimilar materials when a current is injected around a circuit. This is explained by introducing the Peltier coefficient  $\Pi$ , which is a material dependent parameter that is related to the Seebeck coefficient and which describes the amount of thermal energy that is carried per charge carrier. Since the heat current must be continuous across the interface of two materials, if the materials have different Peltier coefficients, the heat will be either rejected or absorbed at the interface, depending on the sign of the difference between the Peltier coefficients and the direction of the current,  $Q_{Peltier} = \Pi I$ , where  $Q_{Peltier}$  is the total heat added or rejected by the system and  $I$  is the current supplied.<sup>21</sup> On the other hand, we can see a third effect on TE materials, the Thomson effect. This is very similar to the Peltier effect. The most important difference between both lies in the fact that the Thomson effect requires a temperature gradient across the semiconductor material along with the current supplied. This means that when the current is supplied and when there is a temperature gradient along the length of the TE material, heat is either absorbed or rejected depending on the direction of the current supplied. Then, the Thomson effect is proportional to the supplied current and the temperature gradient  $Q_{PThomson} = \tau I \Delta T$ , where  $\tau$  is the Thomson coefficient.

Considering both solid-state refrigerators and thermal power, it is necessary to calculate the efficiency of a TE material, given by  $ZT$  computed via eq. (1-1). A modification of this equation is obtained by separating the thermal conductivity,  $k$ , into two parameters,  $k_l$  and  $k_e$ , which represent the thermal conductivities for phonons and electrons, respectively. The effect of phonon and electron coupling is another challenge to study in this work. Therefore, eq. (1-1) is written as

$$ZT = \frac{S^2 \sigma}{k_e + k_l} T \quad (1-1)$$

where  $k_e$  and  $k_l$  are respectively related to the electrons and holes transporting heat and the phonons travelling through the TE material lattice. As we mentioned the total thermal conductivity  $k$  is related to  $k_e$  and  $k_l$  through the relation  $k = k_e + k_l$ . This equation shows that achieving high  $ZT$  values requires a material simultaneously possessing a high Seebeck coefficient and high electrical conductivity, but maintaining a low thermal conductivity ( $k_e$  and  $k_l$ ). The relevance of these transport parameters depends upon one another as a function of the band structure, the carrier concentration and other factors.<sup>53</sup> Figure 1.2 illustrates the three main parameters including the charge carrier concentration.<sup>54</sup> Since the control of carrier concentration through doping is the accessible parameter to tune the TE properties of material. The opposite trends of the Seebeck coefficient and electrical conductivity with increasing carrier concentration result in an optimum doping level.

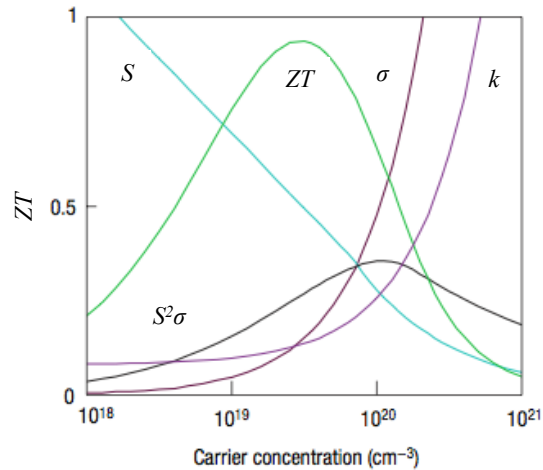


Figure 1.2. Maximizing the efficiency  $ZT$  of a thermoelectric material. The three parameters: thermal conductivity, electrical conductivity, and Seebeck coefficient are involved. Good thermoelectric materials are typically heavily doped semiconductors with a carrier concentration between  $10^{19}$  and  $10^{21}$  charge carriers per  $\text{cm}^3$

One restriction for many industrial applications is the low efficiency ( $ZT < 1$ ). Since 1940, the finding of the best TE material (exhibiting high Seebeck coefficient, high electric conductivity and low thermal conductivity) has been a difficult task. The studies to increase the efficiency have concentrated on the application of different methods to obtain low thermal conductivity. The discovered of many new materials would permit a new promising application in energy solution. Although a lot of effort has been done to increase the  $ZT$ , this is still a promising field to be explored.

### 1.2.2. Density Functional Theory

DFT is one of the most widely used methods for “ab initio” calculations of the structure of atoms, molecules, crystals, surfaces, and their interactions. The simple idea of DFT is the notion that it is possible to replace the dependence on the external potential  $V_n$  by a dependence on the density distribution  $n(r)$  at a particular position in space. In addition, the core concept of

DFT is the observation that, if  $E$  is the lowest possible energy of the system, i.e. the energy of the ground state, then  $E$  is a functional of the electron density only if  $E = F(n)$ . The ground state energy depends only on the  $n(r)$ , which is a function of three variables only. This observation is from Hohenberg and Kohn<sup>55</sup>, and is described through the theorem: *The ground-state energy from Schrödinger's equation is a unique functional of the electron density.* The consequence of this observation is that all that is needed for calculating the total energy  $E$  in the ground state is the electron density,  $n$ .

$$n(r) \xrightarrow{F} E, E = F[n(r)] \quad (1-2)$$

Unfortunately, although the Hohenberg and Kohn theorem proves that a functional of the electron density exists that can be used to solve the Schrödinger's equation, the theorem does not describe what the functional is. Another theorem of Hohenberg and Kohn, defines an important property of the functional: The electron density minimizes the energy of the overall functional is the true electron density corresponding to the full solution of the *Schrödinger equation*. The entire field of DFT rests on the mentioned two fundamental mathematical theorems by Hohenberg and Kohn and the derivation of a set of equations by Kohn and Sham.<sup>56</sup>

Those theorems are based on the following three premises<sup>56</sup>:

1. In the ground state the electron density determines uniquely the external potential of the nuclei,  $V_n, n \rightarrow V_n$ .
2. In any quantum state the external potential,  $V_n$ , determines uniquely the many –electron wavefunction,  $V_n \rightarrow \psi$ .
3. In any quantum state the total energy,  $E$ , is a functional of the many-body wavefunction through,  $\psi \rightarrow E$ .

Combining these three premises, we can infer that the total energy must be a functional of the density  $E = F(n)$ .

The Kohn-Sham approach achieves an exact correspondence of the density and ground state energy of a system consisting of non-interacting electrons and the real many body systems described by the Schrödinger equation. The idea of Kohn and Sham was to split the terms of density,  $n$ , into the kinetic and Coulomb energy of independent electrons, plus an extra term that describe the exchange and correlation energy, and it is defined to include all the quantum mechanical effects that are not included in the known terms (external potential, kinetic energy and Hartree energy), that describes the total energy in the independent electrons approximation.

$$E = F(n) = \int dr n(r) V_n(r) - \sum_i \int dr \phi_i^*(r) \frac{\nabla^2}{2} \phi_i(r) + \frac{1}{2} \iint dr dr' \frac{n(r)n(r')}{|r-r'|} + E_{XC}[n] \quad (1-3)$$

where,

$$\int dr n(r) V_r : \text{External Potential}$$

$$\sum_i \int dr \phi_i^*(r) \frac{\nabla^2}{2} \phi_i(r) : \text{Kinetic Energy}$$

$$\frac{1}{2} \iint dr dr' \frac{n(r)n(r')}{|r-r'|} : \text{Hartree energy}$$

$$E_{XC}[n] : \text{Exchange and correlation energy}$$

If we knew the exchange and correlation energy,  $E_{XC}[n]$ , then we could compute the total energy of the system in its ground state, using the electron density.

### 1.2.3. Boltzmann Transport Theory

The model presented is on approaching the solution of the BTE on the basis of a relaxation time approximation (RTA). There are two categories of transport theories. The first one adopts a wave-like point of view, starts from the dynamic equation of carriers, and the time evolution of carriers' states. On the other hand, the interactions among carriers are added to the calculation usually as perturbations. In TE materials, interactions of carriers among themselves and with impurities are often strong and the coherence effect is suppressed. In this case, it is more convenient to start from the fully incoherent limit, where carriers are treated as quasiparticles and their wave nature is only used in particular situations.

From the perspective of the transport process, and considering that the scattering processes can be described by a relaxation time, the BTE is given by

$$\frac{\partial f}{\partial t} + v \cdot \nabla_r f - \frac{e\epsilon}{\hbar} \cdot \nabla_k f = \left( \frac{\partial f}{\partial t} \right)_{col} \quad (1-4)$$

where  $f(r, k, t)$  is the distribution function in phase space that represents the number of particles occupying a certain state with real-space position  $r$  is a point in the crystal,  $k$  is the Bloch wave vector of an electron,  $t$  is time, and the collision term on the right-hand side contains all the information about the nature of the scattering (carrier interaction), whose exact form is unknown in most practical situations.

With RTA, the BTE can be solved, and the particle number and energy flux can be calculated with the solved distribution function. The TE transport properties have the following form from the BTE with RTA, where the most general form of the relations for electron TE properties such as  $S$ ,  $\sigma$ , and  $k_e$  are expressed by: <sup>57</sup>

$$S_{\alpha\beta}(T, \mu) = \frac{1}{eT\sigma_{\alpha\beta}(T, \mu)} \int \sigma_{\alpha\beta}(\varepsilon)(\varepsilon - \mu) \left[ -\frac{\partial f_0(T, \varepsilon, \mu)}{\partial \varepsilon} \right] d\varepsilon \quad (1-5)$$

$$\sigma_{\alpha\beta}(T, \mu) = \frac{1}{\Omega} \int \sigma_{\alpha\beta}(\varepsilon) \left[ -\frac{\partial f_0(T, \varepsilon, \mu)}{\partial \varepsilon} \right] d\varepsilon \quad (1-6)$$

$$k_{\alpha\beta}^0(T, \mu) = \frac{1}{e^2 T \Omega} \int \sigma_{\alpha\beta}(\varepsilon)(\varepsilon - \mu)^2 \left[ -\frac{\partial f_0(T, \varepsilon, \mu)}{\partial \varepsilon} \right] d\varepsilon \quad (1-7)$$

where  $e$  is the electron charge,  $\Omega$  is the reciprocal space volume,  $\varepsilon$  is the carrier energy,  $f$  is the Fermi distribution function,  $\mu$  is the chemical potential, and  $T$  is the absolute temperature. It is noted here that  $k$  is the electronic thermal conductivity.

#### 1.2.4. X-ray Diffraction Technique (XRD)

XRD represents the most contributive experimental method for structure characterization. XRD is adapted to observe atomic details, as inter-atomic dimensions about 1-2 Å and wavelength in the range of 0.1-1000 Å. X-ray photons from an incident beam are reflected when encountering atoms of the exposed sample, generating a diffracted beam. Over 99% of the X-rays pass through the material without being scattered, then a large number of molecules should be arranged in a well-known spatial configuration, which is recognized as crystal. In 1912, Lawrence Bragg<sup>58</sup> found that the crystalline sample, at certain specific wavelengths and incident angles of the scattering beam, produces intense peaks of reflected radiation. Bragg Law relates the incident wavelength to the scattering angle and the distance between atomic planes of a crystal lattice through  $n\lambda = 2d\sin\theta$ , where a discrete atomic model of a crystal shows the distance  $d$ , and the angle  $\theta$  as a half of the angle between the incident and the scattered beam (Figure 1.3).

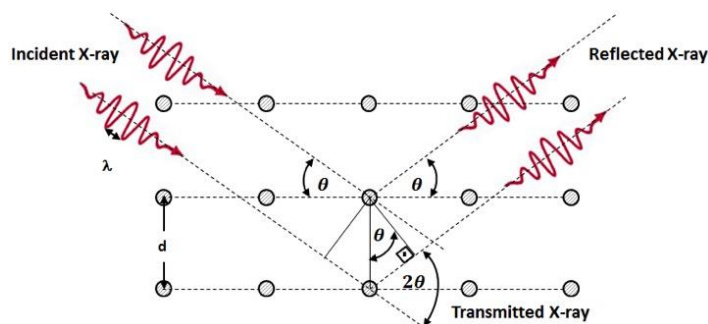


Figure 1.3. Diagram of Bragg's law.<sup>59</sup>

The scattered X-ray from the crystal allows the measurement of a large number of Bragg reflections in a single exposure. The crystals with higher symmetry require fewer diffraction images to cover the entire crystal lattice.

Determination of unknown solids is critical for research in material science, and the XRD technique is the most widely used that allows the identification of unknown crystalline materials (e.g. semiconductors, minerals, inorganic compounds).

#### 1.2.5. Scanning Electronic Microscope Technique (SEM)

SEM is used for observation of sample's surfaces (Figure 2.4). When the sample is irradiated with a fine electron beam, it will interact with atoms of the sample by elastic and inelastic scattering, and secondary electrons are emitted from the sample's surface. Topography of the surface can be observed by two-dimensional scanning of electron probe over the surface and acquisition of an image from the detected secondary electrons. SEM magnifications can reach more than 300,000 X. To produce SEM images the electron beam is swept across the area

being inspected, producing many such signals. These signals are the amplified, analyzed, and translated into images of the topography being inspected. We can obtain several characteristics from the sample using the SEM analysis, such as surface topography, morphology, composition and materials properties, and crystallography information are the most critical when we can characterize materials.

#### 1.2.6. Raman Spectroscopy

Chandrashekhara Venkata Raman in 1928, discovered the phenomena of inelastic scattering of light, known as the Raman effect.<sup>60</sup> This explains the shift in wavelength of a small fraction of radiation scattered by molecules, having different frequency from that of the incident beam. This shift in wavelength depends upon the chemical structure of the molecules responsible for the scattering. In Raman spectroscopy, sample is illuminated with a monochromatic laser beam, which interacts with the molecules of sample and originates a scattered light. The scattered light has a frequency different from that of the incident light (inelastic scattering), which is used to construct a Raman spectrum. Raman spectra arise due to inelastic collision between incident monochromatic radiation and molecules of sample.<sup>61,62</sup> When a monochromatic radiation strikes at sample, it scatters in all directions after its interactions with sample molecules. Raman spectroscopy utilizes this scattered to gain knowledge about molecular vibrations, which can provide information regarding the structure, symmetry, electronic environment and bonding of the molecule, thus allows the quantitative and qualitative analysis of compounds.

### 1.3. Hypothesis of this research

The hypotheses of this research are:

1. The experimental techniques to be use in this research will allow an understanding of the structural and morphological behavior of materials.
2. The numerical simulation using first-principles by DFT and BTE will allow to compute the electrical and thermal properties of materials.

### 1.4. Research challenges and Objectives

The overarching goal of this research is to study the electron and phonon transport properties in bulk and two-dimensional crystalline materials, which could provide important insights to the electronic and thermal transport physics in these materials.

#### 1.4.1. Effect of the Annealing of the Power Factor of Un-Doped Cold Pressed SnSe

SnSe is one of the most studied TE materials in the last decade due its higher ZT value compared with other TE materials. The objective is to determine the structural and morphological characterization of bulk SnSe through XRD and SEM techniques, and to measure the TE properties such as Seebeck coefficient, electrical resistivity and thermal conductivity.

#### 1.4.2. First-Principles Calculations of Thermoelectric Properties of IV-VI Chalcogenides 2D Materials

To study the electronic and thermal behavior of 2D materials, the understanding of electron and phonon transport properties is fundamental. The objective of this part is to compute the TE properties of IV-VI Chalcogenides 2D materials such as SnSe, SnS, GeS, GeSe, SnS<sub>2</sub>,

and SnSe<sub>2</sub>, using first-principles calculations by DFT theory and semi-classical Boltzmann transport.

#### 1.4.3. In-Plane Thermal Conductivity of the Niobium Diselenide from Temperature-Dependent Raman Spectroscopy

The main challenge in this study is determining the in-plane thermal conductivity of thin film NbSe<sub>2</sub>. The objective of this part is to determine the in-plane thermal conductivity of NbSe<sub>2</sub> from experimental study using temperature-dependent Raman spectroscopy, and my role is to perform a simulation study using first-principles calculations by DFT theory and semi-classical Boltzmann transport.

#### 1.5. Methodology

The methodology proposed in this research is separated in two parts. The first part consists of an experimental study of bulk SnSe, where we characterize the material using XRD and SEM techniques, and then we obtain the structural and morphological properties respectively. In addition, we determine the TE properties of this compound, measuring directly the Seebeck coefficient and the electrical resistivity. The thermal conductivity was measure by the laser flash diffusivity technique. The second part was developed through a theoretical and numerical work, where the goal is to determine and analyze the electronic and thermal behavior of the monolayer materials such as SnSe, SnS, GeS, GeSe, SnS<sub>2</sub>, SnSe<sub>2</sub>, and NbSe<sub>2</sub>. The electronic behavior was developed through the calculus of the band structures and density of states, and the TE properties such as Seebeck coefficient, electrical conductivity and electronic thermal conductivity, using first-principles calculations by DFT, through the DFT Quantum Espresso and semi-classical Boltzmann transport approach implemented in the BoltzTraP package.<sup>57</sup> The thermal

conductivity, was obtained by computing the harmonic force constants using the Quantum Espresso <sup>63</sup> based on the DFPT, and to calculate the cubic force constants, we use the `thirdorder.py` script from ShengBTE program, <sup>64</sup> based on the iterative solution of phonon BTE.

The expected results of this thesis are:

1. The microstructural effect will play a predominant role on the TE performance as compared with the effect of morphological and chemical characteristics of the material.
2. A good relation for both thermal and electrical parameters (thermal conductivity, electrical conductivity and Seebeck coefficient), such as low thermal conductivity, high electrical conductivity and high Seebeck coefficient, in order to improve the  $ZT$ .

## 1.6. Principal results and conclusions

The overall results, discussion and conclusions obtained from this research are presented in Chapter 5 at the end of this thesis. However, detailed descriptions of the results are presented in the following chapters.

In Chapter 2, we studied the electronic and thermal transport properties of an un-doped cold-pressed SnSe. We characterized the sample from structural and morphological techniques, and we obtain the TE properties. The performance of this compound, called figure of merit,  $ZT$ , that involves all the TE properties, reaches a value of 0.11 at 772 K.

In Chapter 3, DFT and the Boltzmann transport model are used to calculate the TE properties of monolayer materials. We determine the electronic band structure and TE properties without and with Spin Orbit Coupling (SOC). We notice a small effect of SOC over the band gaps for all materials. The TE properties are calculated at different doping levels, and it was found that the SnSe has the largest  $ZT$  disregard the doping level.

In Chapter 4, we report a simulation study using first-principles by DFT and BTE calculations to compute the phonon properties and the lattice thermal conductivity of thin film NbSe<sub>2</sub>. The obtained results 13.5 W/mK, are in good agreement with the in-plane thermal conductivity obtained from an experimental study done by our collaborators, where the thermal conductivity reaches  $14 \pm 5$  W/mK at room temperature

### 1.7. Organization of the Thesis

The thesis is organized as follows. In Chapter 2, we describe the experimental research to determine the structural and morphological characterization of bulk SnSe, as well as the TE properties. Chapter 3 presents a simulation study using first-principles calculations by DFT of six compounds to determine the band structures and the thermoelectric properties. Chapter 4 presents a simulation study using first-principles calculations by DFT, and BTE calculations of thermal conductivity of niobium diselenide. Chapter 5 summarizes the thesis findings and potential future directions.

## CHAPTER 2: EFFECT OF THE ANNEALING ON THE POWER FACTOR OF UN-DOPED COLD PRESSED SnSe

### 2.1. Background

Tin Selenide (SnSe), a thermoelectric material of the Chalcogenide family, has attracted tremendous interest in the past few years due to its unprecedented thermoelectric figure-of-merit,  $ZT$ , of 2.6. In this work we have carried out an experimental study of the impact of annealing on the thermoelectric properties of polycrystalline SnSe formed by cold-pressing un-doped SnSe powders with a Hall carrier concentration of  $5.37 \times 10^{17} \text{ cm}^{-3}$ . The crystalline structure and morphology of the samples are characterized and properties, including electrical conductivity, Seebeck coefficient and thermal conductivity, are measured. It is found that thermal annealing has a large impact on both the microstructure and the thermoelectric properties. Notably, annealing leads to re-alignment of crystalline domains, increase in Seebeck coefficient by a factor of as much as 3, and increase in the electrical conductivity. A peak  $ZT$  of 0.11 was achieved at 772 K, which is smaller than un-doped polycrystalline SnSe.

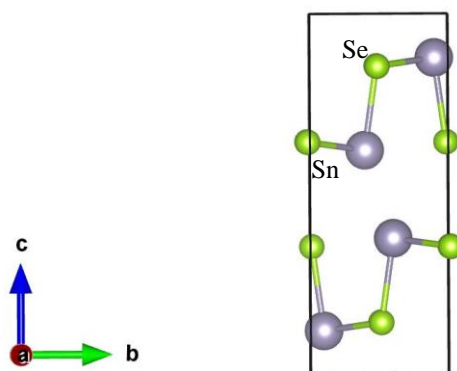


Figure 2.1. Illustration of orthorhombic crystal structure of SnSe

## 2.2. Experimental Details

### 2.2.1. Sample preparation

Polycrystalline powder of SnSe (99.995% trace metals basis) was obtained from Sigma Aldrich (CAS Number 1315-06-6). Disk-shaped SnSe tablets were prepared by cold-pressing of the powder at room temperature under a uniaxial pressure of  $25.47 \text{ kgf/mm}^2$  using an oleo hydraulic press. SnSe tablets with dimensions of 8 ~ 10 mm diameter and 1 ~ 1.28 mm thickness were obtained. After the cold-pressing process, the samples were characterized by XRD and SEM before and after an annealing process. Electrical transport properties, such as Seebeck coefficient and electrical conductivity, were measured in-situ while thermal annealing was performed on the samples. The SnSe tablet was placed inside the Linseis LSR-3 system, and heated from RT to 500 °C with a 10 K/min heating rate under Helium controlled atmosphere, followed by cooling back to RT. This procedure was carried out for each measure for six times to observe the gradual change of thermoelectric properties with the annealing process.

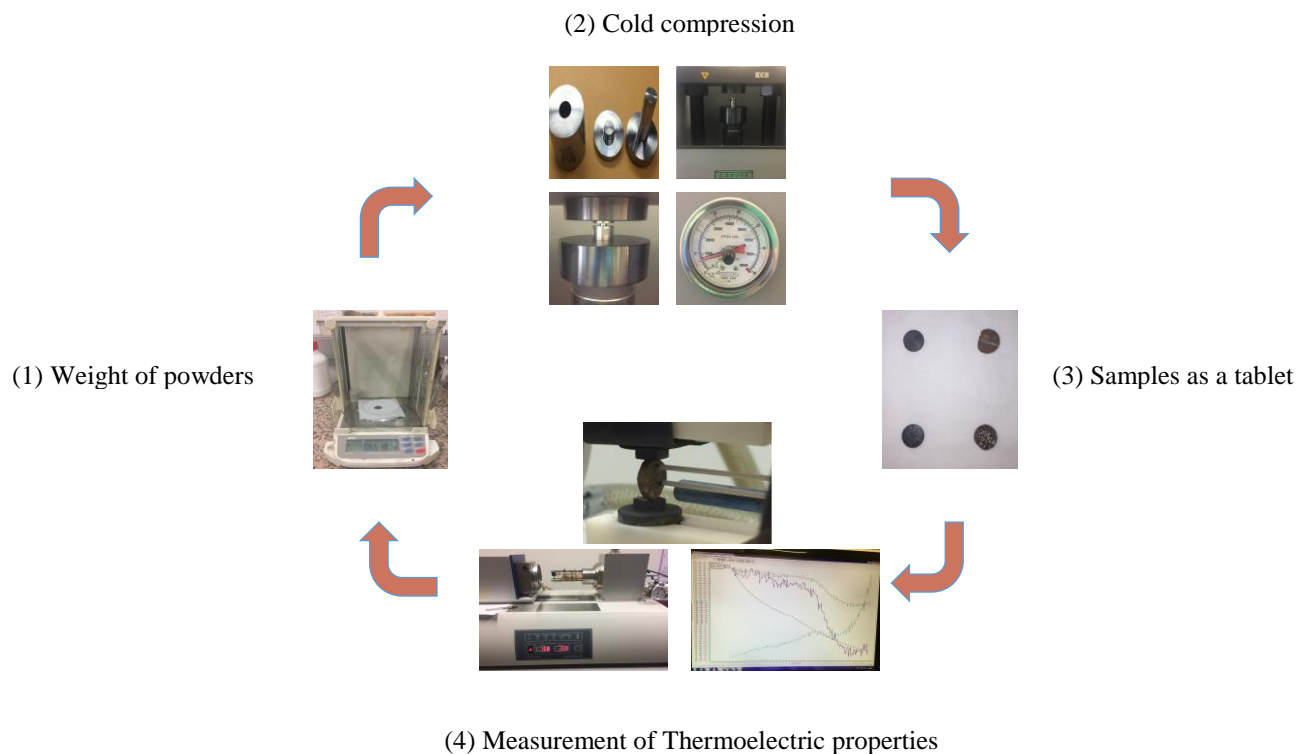


Figure 2.2. Flow of samples' preparation and thermoelectric properties' measurement

### 2.2.2. Sample Characterization

### 2.2.3. X-ray Diffraction (XRD)

Powder XRD analysis was carried out to characterize the crystallinity and phase composition at room temperature using a Bruker D-8 Advanced Diffractometer with a long fine focus ceramic X-ray tube and a copper anode ( $\lambda(\text{CuK}\alpha) = 1.54 \text{ \AA}$ ). The analysis was performed in the Bragg-Brentano ( $\theta - 2\theta$ ) geometry using the SnSe tablet in a rotating holder with XRD.

#### 2.2.4. Scanning Electron Microscopy (SEM)

Microstructures of the sample was characterized using two types of electron microscopes: a FEI Quanta 650FEG ESEM and a FEI scanning electron microscope, both equipped with an energy dispersive x-ray spectroscopy system (EDS) at an accelerating voltage of 2, 5, 10 and 15 kV and using secondary electron detectors.

#### 2.3. Measurement of Transport Properties

The transport properties were measured using three different systems. The Seebeck coefficient and electrical resistivity were measured in-situ while the annealing was performed on the SnSe tablet using a Linseis LSR-3 system with a static DC method. Then, the Hall coefficient and electrical conductivity data were obtained ex-situ after the annealing process by using the Van der Pauw method with an Ecopia HMS-5000 Hall Effect measurement system. These electrical conductivity values were used to correct the electrical resistivity values obtained from the Linseis LSR-3 system. Such a correction is necessary for the electrical resistivity, because the Linseis LSR-3 system measures the resistance, and then calculates the resistivity using the width and length of the tablet. This calculation can be inaccurate since there is no way to measure the area and length where the current flows. Thus, the values of electrical resistivity obtained by Linseis LSR-3 system is off by a fixed factor, which can be obtained by comparing the resistivity from the Linseis LSR-3 system and the conductivity from the Ecopia HMS-5000 system.

From the Hall coefficient, the carriers concentration of the SnSe samples can be calculated as:

$$n = \frac{1}{R_H q} \quad (2-1)$$

where  $n$  is the carrier concentration in  $\text{cm}^{-3}$ ,  $R_H$  is the Hall coefficient in  $\text{cm}^3/\text{C}$ , and  $q$  is the electron charge of  $1.6 \times 10^{-19}$  C.

The SnSe sample is then cut into a 6 mm square, and the bulk thermal diffusivity ( $h$ ) was measured using the laser flash method<sup>66</sup> on a Netzsch Laser flash system (model LFA 457) under nitrogen purge. The laser flash technique allows non-contact measurement at the same temperature range (RT - 500°C) as that used in electrical property measurements.

The specific heat ( $C_p$ ) of the sample was needed for calculating thermal conductivity from the thermal diffusivity ( $h$ ), and it was measured using a differential scanning calorimetry (DSC) thermal analyzer (DSC Q2000). The volumetric density ( $\rho$ ) was calculated using the measured dimensions and its weight. Finally, the total thermal conductivity was calculated from the expression:  $k = C_p \rho h$ .

#### 2.4. Crystallographic Features

Figure (2.3) shows the XRD diffractograms from the cold-pressed SnSe tablet before annealing (Figure 2.3 a) and after annealing (Figure 2.3 b). The results of XRD were analyzed by the X'Pert High Score software package and are compared with the standard card file (JCPDS #00-048-1224, Fig. 3c). We notice a change of the strongest peak before and after annealing. Before annealing, the strongest peak (111) matches well with the standard card. However, after annealing, the strongest peak changes to the (400) peak. The ratio of  $I_{(400)}$  to  $I_{(111)}$  is 3.74 which, compared with the value of 0.52 for the standard card, suggests an excellent preferred grain orientation.<sup>19,67,68</sup> It is interesting to find out that the relative peak heights of (111) and (400) before and after annealing of our cold-pressed sample qualitatively agree with the XRD features of hot-pressed SnSe with the incident X-Ray from different directions<sup>68</sup>: before annealing our sample shows a XRD feature similar to that of the hot-pressed SnSe with the incident X-Ray along the press direction, while after annealing our sample shows a XRD feature similar to that of the hot-pressed SnSe with the incident X-Ray perpendicular to the press direction. Such an

observation suggests that annealing of our cold-pressed sample may have led to realignment of the crystalline domains.

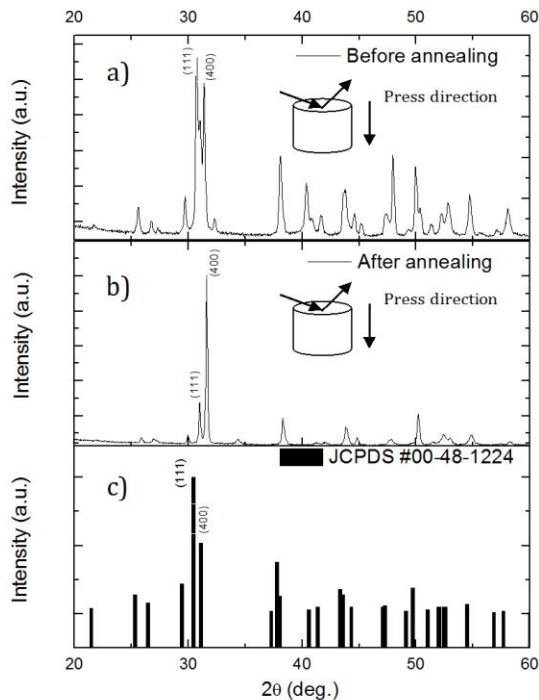


Figure 2.3. (a) Sample before annealing, (b) sample after annealing, and (c) reference XRD pattern of SnSe<sup>65</sup>

## 2.5. Microstructure

Figure (2.4) shows the SEM images of the top of un-doped SnSe bulk sample. Figures (2.4 a) and (2.4 b) show the center and edge of the sample before annealing while Figures (2.4 c) and (2.4 d) show the center and the edge of the sample after annealing. Figures (2.4 a) and (2.4 b) show the surface morphology from the tablet after compactation of the SnSe commercial powder under a uniaxial pressure of 25.47 kgf/mm<sup>2</sup>. We believe that a higher compactation grade was obtained at the center of the tablet than at its edges where powder is slightly more unbundled with some particles of different sizes not completely embedded in the Tablet, as shown in Figure

(2.4 b). This fact also is revealed when the tablet is manipulated after cold-pressing since its edges tend to crumble under small stresses. The annealing process allows a better cohesion of the individual particles, increasing the strength of the whole tablet; however, its edge also looks different as compared with the center of the tablet due to different compactation grade of the as-prepared sample, as revealed in Figures (2.4 c) and (2.4 d). Even cracks are detected from Figure (2.4 d).

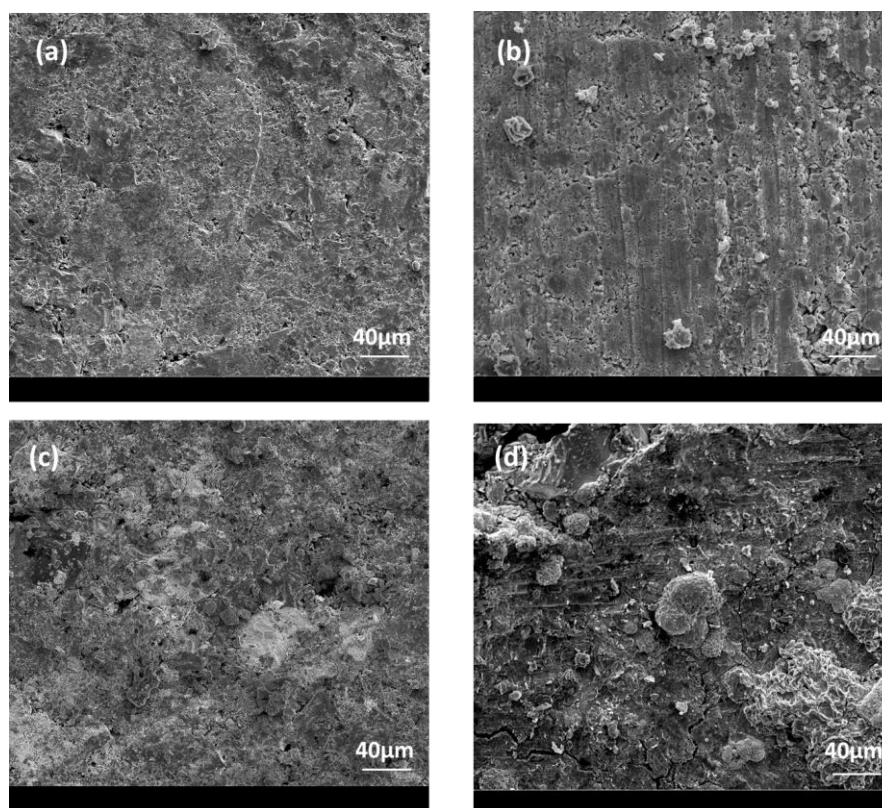


Figure 2.4. SEM images acquired from an un-doped SnSe tablet. (a) center and (b) edge of the sample before annealing. (c) center and (d) edge of the sample after annealing

## 2.6. Thermoelectric Properties

### 2.6.1. Seebeck Coefficient

All measured Seebeck coefficients were positive indicating the p-type behavior from the SnSe tablet. The annealing has a large impact in the Seebeck coefficient, consistently improving their value by as much as three times. As seen in Figure (2.5 a), the highest value is  $448 \mu\text{V K}^{-1}$  at RT at the sixth measurement (i.e., the sample was exposed to six thermal annealing cycles) compared to the starting value of  $150 \mu\text{V K}^{-1}$  of the un-annealed sample at RT. As a result, we can conclude that thermal annealing has a positive effect on the Seebeck coefficient. However, despite improving its value, it should be noted that it is a little lower than previous results for un-doped hot-pressed polycrystalline SnSe samples.<sup>16–20,67,69</sup> One possible explanation is linked with the level of carrier concentration at room temperature. The magnitude of the Seebeck coefficient can be tailored suitably by tuning the carrier concentration. The interrelationship between Seebeck coefficient and carrier concentration can be seen in a model of electron transport<sup>54</sup>, where the carrier concentration is inversely proportional to the Seebeck coefficient, i.e. with higher values of carrier concentration lower values of Seebeck coefficient are expected.

In the present work, we obtained a value of  $5.37 \times 10^{17} \text{cm}^{-3}$  for carrier concentration at room temperature, which is slightly higher than the values reported at room temperature for un-doped SnSe<sup>16,19,68,69</sup>, which would explain the trend of the Seebeck coefficient as a function of temperature.

We state that pressing at high temperature (hot-pressed) will combine the annealing effect with the pressing force to form better contacts among the grains, probably with low angle grain boundaries and a lower dislocations density and, thus, enhance electrons transport which, in fact, would benefit to the Seebeck coefficient value.<sup>68</sup>

When the temperature increases within one annealing cycle, the Seebeck coefficient generally decreases until 675 K and then increases, with the exception for the first cycle, where it firstly increases and then decreases followed by the final increase. The overall trend of our measured Seebeck coefficient as a function of temperature is opposite to that of the literature measurements on hot-pressed annealed Ag-doped<sup>16</sup> or Na-doped<sup>68</sup> samples, where the coefficient firstly increases and then starts to decrease. Only highly Ag-doped SnSe samples (7%) show a behavior similar to ours. The increase and then decrease trend is usually due to bipolar conduction contributed from minority carrier's excitation.

After careful observation, we see that the slope of the decrease trend in the Seebeck coefficient becomes smaller until around 550-600 K. For hot-pressed annealed SnSe samples, the peak Seebeck coefficient was also observed around this temperature range<sup>16</sup>. The major difference between our measurements and those by Chen et al.,<sup>16</sup> is that we are effectively annealing the sample on-the-fly whereas Chen et al. annealed the sample for a sufficiently long time (72 hours at 800 K) before the measurement. Although the Seebeck coefficient behavior from our measurements possibly reflects the bipolar effect convoluted with the internal microstructure change of the sample, a detailed correlation between the microstructure changes and Seebeck coefficient values is not currently understood and it needs further investigation.

### 2.6.2. Electrical Conductivity

The Hall carriers concentration of un-doped SnSe tablet at room temperature was measured to be around  $5.37 \times 10^{17} \text{ cm}^{-3}$ , which is consistent with previously reported values for un-doped SnSe.<sup>16,19</sup> Within each annealing cycle, the electrical conductivity of our sample increases with temperature, which is due to the increase in charge carrier populations due to thermal activation. Different from that seen for the Seebeck coefficient, the effect of annealing

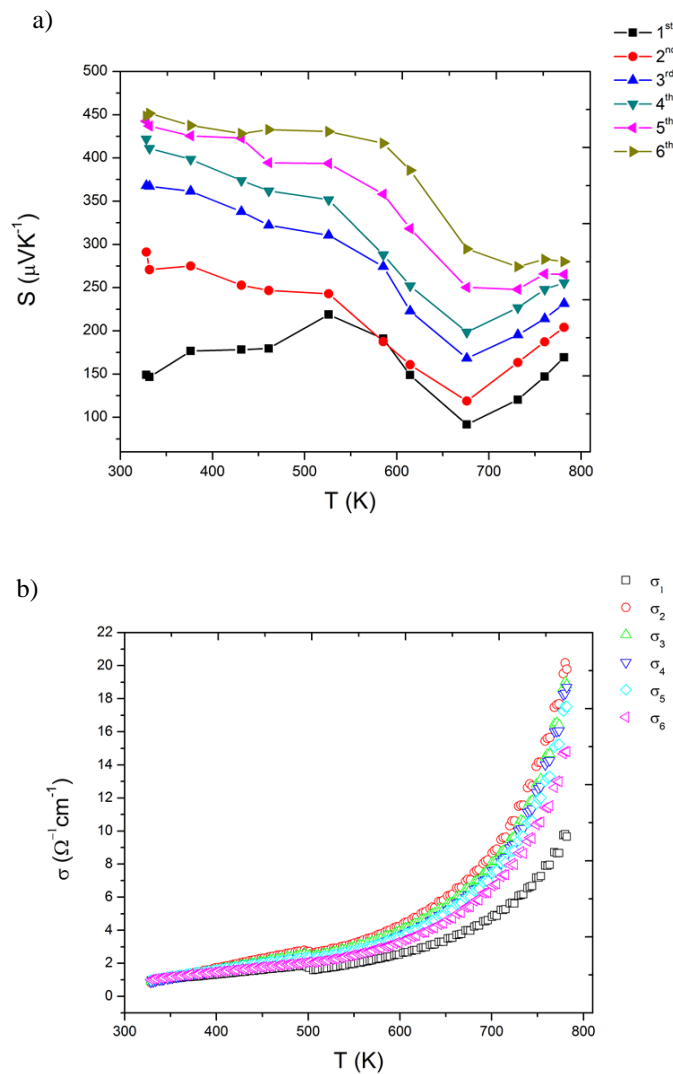
on the electrical conductivity is, however, non monotonic. The second annealing cycle leads to a uniform increase in conductivity over the whole temperature range compared to the first cycle, while all cycles after the second one lead to a gradual decrease in conductivity (Figure 2.5 b). The increase in conductivity from the first to the second annealing cycle might be attributed to both the improvement of crystal structure and merge of some loose grain boundaries as well as to a low in the dislocations density. However, the mechanism of the decreasing trend after the second cycle is not currently clear. One explanation for the little decrease of electrical conductivity after the second annealing cycle could be attributed to the decreasing of Hall mobility due to the grain boundary scattering<sup>70</sup>, and the increasing of carrier-carrier scattering<sup>68</sup>.

Also, on the other hand, it is possibly related to crystal domain re-alignment. Chere et al.<sup>68</sup> found that the electrical conductivity is anisotropic with respect to the press direction and thus to the crystal alignment direction. As shown previously in the XRD spectra (Figure 1), annealing could lead to crystal re-alignment (texturization), and this might have led to the change in conductivity. Such a crystalline direction preference, however, does not have a significant effect on the Seebeck coefficient as also shown in Ref.<sup>68</sup>. The improvement in Seebeck coefficient should be attributed to the improvement in the crystalline and grain boundary quality, which is the same reason for the increase in electrical conductivity from the first to the second annealing cycle. It should be noted that the range of the electrical conductivity measured in our sample is consistent with previously reported values of un-doped polycrystalline SnSe.<sup>16,17,19,20,67-69</sup>

### 2.6.3. Power Factor

Power Factor (PF) is calculated from Seebeck coefficient and electrical conductivity as  $S^2\sigma$ . Due to the quadratic relationship between PF and  $S$ , the improvement in the Seebeck

coefficient over different annealing cycles dominates the behavior of PF despite the decrease in electrical conductivity from cycle two through cycle six. Figure (2.5 c) shows the behavior of PF, and how it improves after each annealing cycle. The maximum value of PF found is  $1.16 \mu\text{W cm}^{-1} \text{K}^{-2}$  at 782 K which, despite the improvement, is still much smaller than the reported values of hot-pressed annealed polycrystalline un-doped SnSe ( $2\text{-}5 \mu\text{W cm}^{-1} \text{K}^{-2}$  at  $\sim 780 \text{K}$ ).<sup>16,19,67,68</sup>



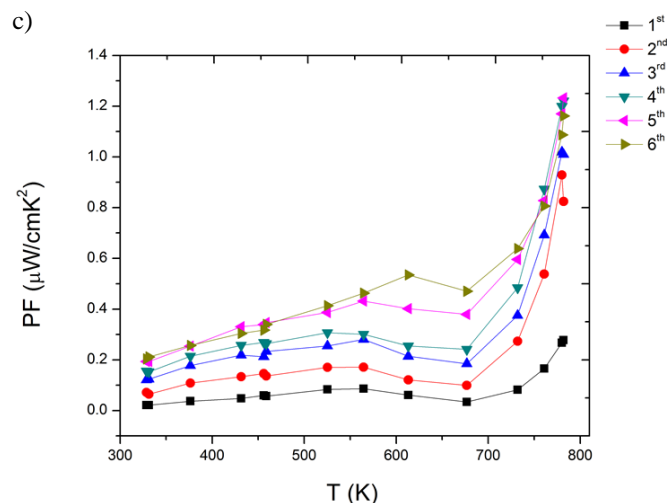


Figure 2.5. (a) Seebeck coefficient ( $S$ ) values, (b) electrical conductivity ( $\sigma$ ), and (c) power factor (PF) as a function of temperature of un-doped polycrystalline SnSe

#### 2.6.4. Thermal Conductivity

The thermal conductivity of un-annealed cold-pressed SnSe sample measured using the laser flash method is shown in Figure (2.6 a). It is found that the thermal diffusivity values are similar to those of hot-pressed annealed SnSe.<sup>68</sup> Although, we did not perform measurements of annealed SnSe sample, we have also measured the specific heat and found very similar results compared to the hot-pressed annealed SnSe in the temperature range covered by our equipment (RT-375 °C).<sup>68</sup> We then use the heat capacity from Ref.,<sup>68</sup> and our measured volumetric density to calculate the thermal conductivity.

It is found that our measurement of thermal conductivity presented in Figures (2.6 b) and (2.6 c) is  $1.14 \text{ W m}^{-1}\text{K}^{-1}$  at RT, which is greater than other un-doped SnSe samples<sup>16</sup>, Na-doped samples (1.5% and 3%)<sup>68</sup>, and single crystals<sup>14</sup> but lower than Ag-doped samples (7%, 5%, and 3%)<sup>16</sup>. However, the behavior of the thermal conductivity as a function of temperature is similar to the depicted by the Ag-doped sample (1%)<sup>16</sup> (Figure 2.6 c).

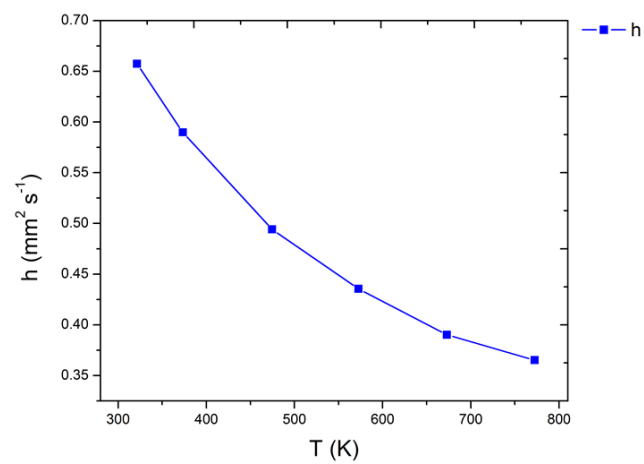
In addition, due to high resistivity, the electronic thermal conductivity was found to be negligible<sup>16</sup>. We have confirmed this using the Wiedemann-Franz law (Figure 6b).

On the other hand, the thermal conductivity decreases slowly with temperature with a scaling relation of  $T^{-0.577}$  (Figure 2.7), which is within the range of the scaling relations in Ref.<sup>17,68</sup> However, our value of scaling relation is smaller than that indicated by Chen<sup>71</sup>, where the high temperature dependence, a result of the phonon-phonon scattering, is often between -1 and -1.5.

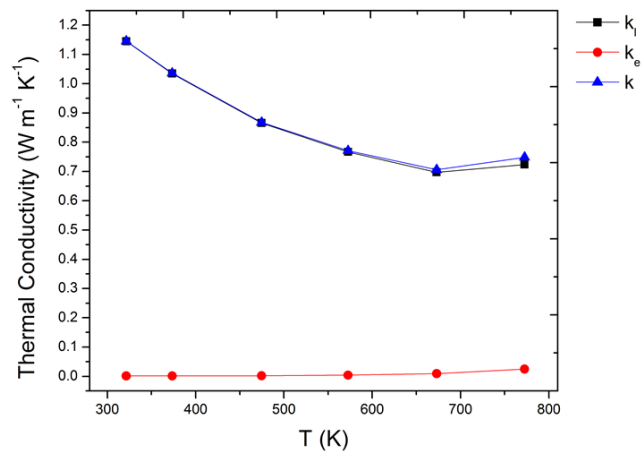
One possible explanation is that there are so many grain boundaries, with scattering phonons, such that the interfacial thermal conductance normally increases with temperature as higher temperatures excite more phonons (i.e., specific heat increases), and thus there are more phonons that participate in the interfacial thermal transport.<sup>72</sup> Also, enhanced anharmonic phonon scattering can also improve interfacial thermal transport.<sup>73</sup> This increase in interfacial thermal transport will act on top of the reduction of thermal conductivity due to three-phonon scattering and thus effectively makes the slope smaller than 1.

Figure (2.6) shows the decreasing trend of thermal conductivity, which indicates anharmonic phonon scattering- dominated mechanism for thermal transport.

a)



b)



c)

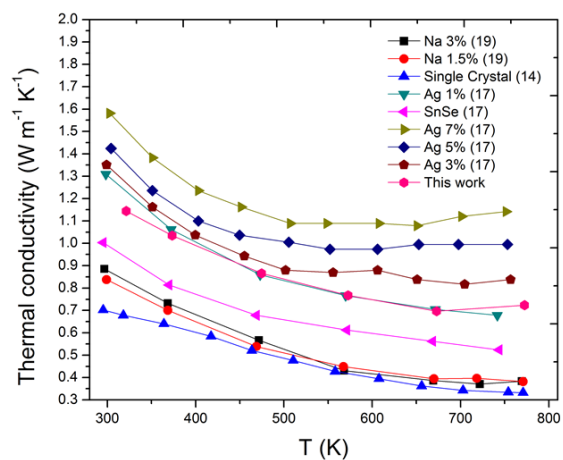


Figure 2.6. (a) Thermal diffusivity ( $h$ ), (b) lattice ( $k_l$ ), electronic ( $k_e$ ), and thermal ( $k$ ) conductivity of un-doped SnSe polycrystalline, and (c) thermal conductivity of this work compared with references

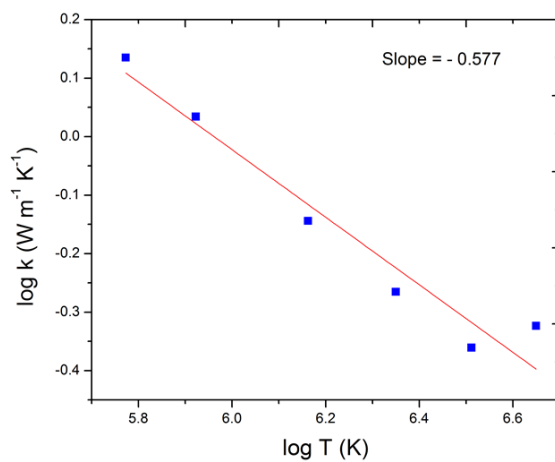


Figure 2.7.  $\log k_l - \log T$  of un-doped polycrystalline SnSe sample

### 2.6.5. Figure of Merit

The figure of merit  $ZT$  is obtained from Eq. 1, and we notice the performance of  $ZT$  considering the transport properties ( $S^2\sigma$ , and  $k_l$ ) for the last (i.e., sixth) measurement. The value obtained predict a peak  $ZT$  of 0.12 at 772 K (Figure 2.8), which is lower than previously reported of un-doped polycrystalline SnSe<sup>19,67</sup>, Ag-doped SnSe samples (1%, 3%, and 5%)<sup>16</sup>, and Na-doped SnSe samples<sup>68</sup>. However, our value behaves like that of Ag-doped SnSe sample (7%)<sup>16</sup>.

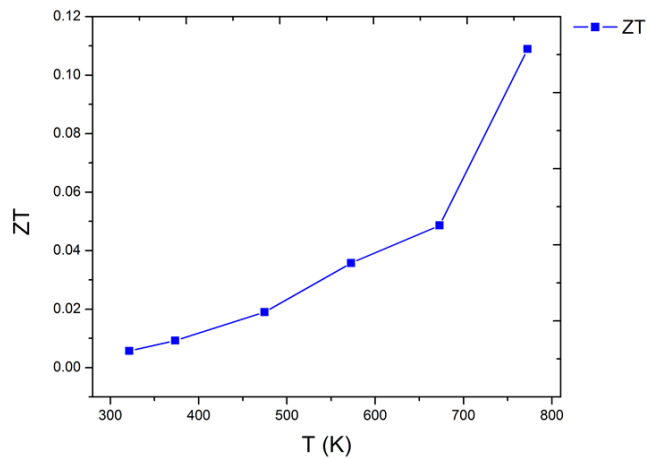


Figure 2.8. Figure of merit ( $ZT$ ) as a function of temperature of un-doped polycrystalline SnSe

## CHAPTER 3: FIRST-PRINCIPLES CALCULATIONS OF THERMOELECTRIC PROPERTIES OF IV-VI CHALCOGENIDES 2D MATERIALS

### 3.1 Background

A first-principles study using density functional theory and Boltzmann transport theory has been performed to evaluate the thermoelectric properties of a series of single layer 2D materials. The compounds studied are SnSe, SnS, GeS, GeSe, SnSe<sub>2</sub>, and SnS<sub>2</sub>, all of which belong to the IV-VI Chalcogenides family. The first four compounds have orthorhombic crystal structures, and the last two have hexagonal crystal structures. Solving a semi-empirical Boltzmann transport model through the BoltzTraP software, we compute the electrical properties, including Seebeck coefficient, electrical conductivity, power factor and the electronic thermal conductivity, at three doping levels corresponding to 300 K carrier concentrations of  $10^{18}$ ,  $10^{19}$  and  $10^{20}$  cm<sup>-3</sup>. The spin orbit coupling (SOC) effect on these properties is evaluated and is found not to influence the results significantly. First-principles lattice dynamics combined with the iterative solution of phonon Boltzmann transport equations are used to compute the lattice thermal conductivity of these materials. It is found that these materials have narrow band gaps in the range of 0.75-1.58 eV. Based on the highest values of figure-of-merit  $ZT$  of all the materials studied, we notice that the best thermoelectric material at the temperature range studied here (300-800K) is SnSe.

### 3.2 Computational details

The methodology used for our calculations is based on first-principles density functional theory<sup>74</sup> (DFT) calculations and Boltzmann transport theory. The structures of the studied 2D materials are first optimized using DFT calculations and then the electron transport properties are calculated using DFT program Quantum Espresso<sup>75</sup> and the semi-classical Boltzmann transport approach implemented in BoltzTraP.<sup>57</sup> The thermal conductivity values are calculated using the iterative solution of phonon Boltzmann transport equation (BTE) using the ShengBTE<sup>64</sup> code with force constants calculated from Quantum Espresso.

For all DFT calculations, the generalized gradient approximation (GGA) of Perdew, Burke, and Ernzerhof (PBE) are used for the exchange-correlation functional.<sup>76</sup> The kinetic energy cutoff of the wave functions is set to 50 Ry for all calculations. The Monkhorst-Pack  $k$ -mesh of  $8 \times 8 \times 1$  is used to sample the first Brillouin Zone. In the electronic band structure calculation, a finer mesh of  $25 \times 25 \times 1$  is used. To simulation monolayers, a large vacuum space of at least 10 Å is left in the  $z$ -direction to prevent the interactions between the layer and its periodic images in the cross-plane direction. The optimized lattice parameters and their comparison to values reported in the literature are presented in Table 1.

Table 1. Literature and our optimized lattice parameters for all the 2D materials studied

Comp.	Phase	Literature values		Our optimized values	
		parameters (Å)		parameters (Å)	
SnSe	Pnma	a	4.44	a	4.46
		b	4.15	b	4.29
SnS	Pnma	a	4.30	a	4.39
		b	3.65	b	4.08
GeSe	Pnma	a	4.38	a	4.39
		b	3.95	b	3.96
GeS	Pnma	a	4.30	a	4.29
		b	3.64	b	3.68
SnS <sub>2</sub>	P3ml	a	3.64	a	3.64
SnSe <sub>2</sub>	P3ml	a	3.81	a	3.89

\*Source of literature values: SnSe<sup>77</sup>, SnS<sup>77</sup>, GeSe<sup>78</sup>, GeS<sup>79</sup>, SnS<sub>2</sub><sup>77</sup>, SnSe<sub>2</sub><sup>77</sup>

Once the structures are optimized, we continue to calculate the electronic transport properties and the lattice thermal conductivity. The flow chart of these calculations, their corresponding input and output parameters and the programs used are schematically shown in Figure (3.1).

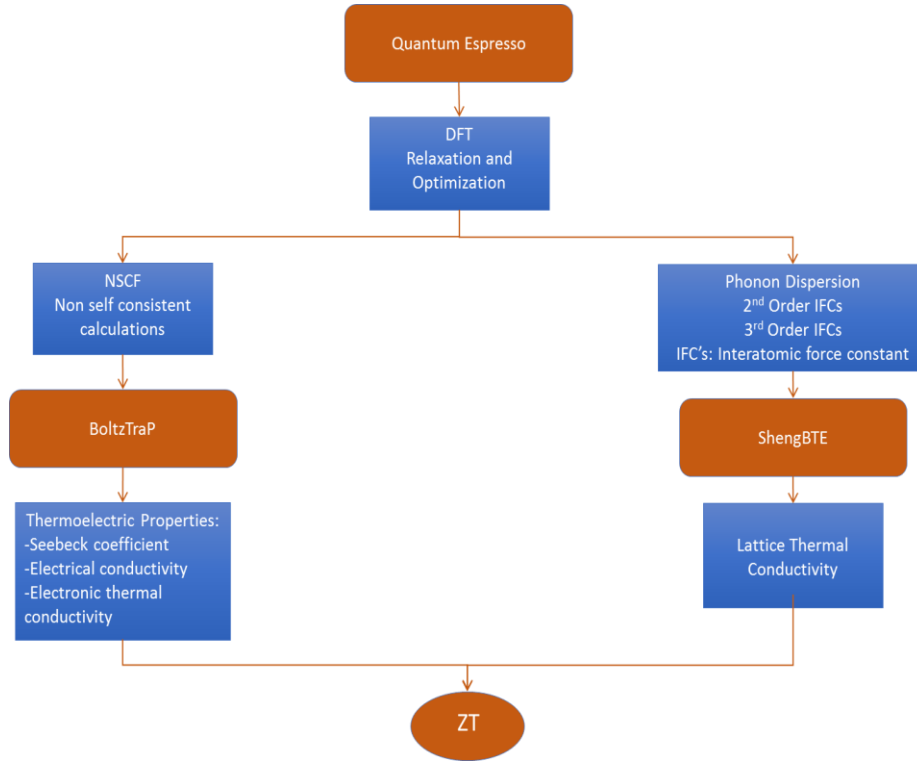


Figure 3.1. Schematic of the flow chart for TE properties and lattice thermal conductivity calculations

To obtain the electronic transport properties, including electrical conductivity, Seebeck coefficient and electronic thermal conductivity, the electron band structure and density of states (DOS) are first calculated in the DFT framework. Then, the band structures are then input into the BoltzTraP package,<sup>57,80</sup> which uses a Fourier expansion scheme to fit the band structures for transport property calculations. In the semi-classical transport theory, the Seebeck coefficient, electrical conductivity and electronic thermal conductivity transport tensors are expressed as:<sup>57</sup>

$$S_{\alpha\beta}(T, \mu) = \frac{1}{eT\sigma_{\alpha\beta}(T, \mu)} \int \sigma_{\alpha\beta}(\varepsilon)(\varepsilon - \mu) \left[ -\frac{\partial f_0(T, \varepsilon, \mu)}{\partial \varepsilon} \right] d\varepsilon \quad (3-1)$$

$$\sigma_{\alpha\beta}(T, \mu) = \frac{1}{\Omega} \int \sigma_{\alpha\beta}(\varepsilon) \left[ -\frac{\partial f_0(T, \varepsilon, \mu)}{\partial \varepsilon} \right] d\varepsilon \quad (3-2)$$

$$k_{\alpha\beta}^0(T, \mu) = \frac{1}{e^2 T \Omega} \int \sigma_{\alpha\beta}(\varepsilon)(\varepsilon - \mu)^2 \left[ -\frac{\partial f_0(T, \varepsilon, \mu)}{\partial \varepsilon} \right] d\varepsilon \quad (3-3)$$

where  $e$  is the electron charge,  $\Omega$  is the reciprocal space volume,  $\varepsilon$  is the carrier energy,  $f$  is the Fermi distribution function,  $\mu$  is the chemical potential, and  $T$  is the absolute temperature. It is noted here that  $k$  is the electronic thermal conductivity.

On the other hand, the conductivity tensor ( $\sigma_{\alpha\beta}(\varepsilon)$ ) as a function of energy is expressed as:

$$\sigma_{\alpha\beta}(\varepsilon) = \frac{1}{N} \sum_{i,k} \sigma_{\alpha\beta}(i, k) \frac{\delta(\varepsilon - \varepsilon_{i,k})}{d\varepsilon} \quad (3-4)$$

where  $N$  is the number of k-points in the reciprocal space.

The relaxation time  $\tau$  depends, in principle, on both the wave vector and frequency. However, BoltzTraP treats the relaxation time to be a constant, which has been shown to be a reasonable assumption.<sup>57</sup> Our calculations for all TE properties were performed with a constant relaxation time approximation  $\tau = 1.0 \times 10^{-14}$  s, which is the value often chosen in similar calculations.<sup>57,81-83</sup>

To obtain the thermal conductivity, we calculate the harmonic force constants using the density functional perturbation theory (DFPT) as implemented in Quantum Espresso with a q-point grid size of  $8 \times 8 \times 1$ . Then, a finite difference method based on supercell calculations (cell size of  $4 \times 4 \times 1$ ) is used to extract the cubic force constants. A cutoff radius of 5 Å is used for the cubic force constant calculation based on convergence test. These force constants are then fed into the ShengBTE program<sup>84</sup> to calculate thermal conductivity based on an iterative solution of phonon BTE. A  $q$ -mesh of  $30 \times 30 \times 1$  is used for all thermal conductivity calculations.

We need to specially emphasize the choice of the thicknesses of the 2D materials used for calculating the electrical conductivity, electronic thermal conductivity, and lattice thermal

conductivity. We used a thickness of 6.0 Å (the interlayer distance of bulk SnSe crystal) for all calculations to enable fair comparison of the properties among all the two materials. In 2D materials, thickness is not well defined, but the concept of electrical and thermal conductivity, which are 3D intensive property, require their quantities to be independent of the cross-sectional area of the material. However, since all electron and heat has to go through the single layer structures, no matter how “thick” or “thin” the structure is, the same thickness should be used to remove any artifact in comparing the electron and thermal transport ability of different 2D materials when using the 3D property – electrical and thermal conductivity. Such a factor has been discussed in details in previous papers.<sup>85,86</sup>

The 2D TE compounds simulated in this work have two kinds of crystal structures, including orthorhombic and hexagonal.<sup>81,87–89</sup> Figure (3.2 a) shows the orthorhombic crystal structure for compounds such as SnSe, SnS, GeSe and GeS in the Pnma-phase (#62),<sup>81,87,89,90</sup> and Figure (3.2 b) shows the hexagonal crystal structure for compounds such as SnSe<sub>2</sub> and SnS<sub>2</sub> in the P3m1-phase (#164).<sup>88,91,92</sup> For each simulation, only one layer was considered, where the number of atoms per primitive cell is 4 for the orthorhombic crystal structure and 3 for the hexagonal crystal structure.

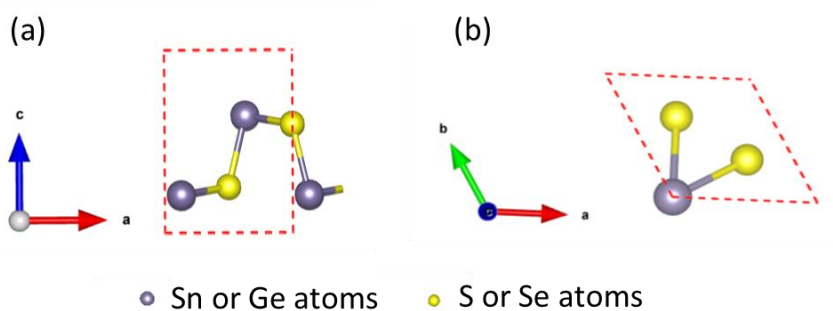


Figure 3.2. Crystal structures of (a) orthorhombic and (b) hexagonal materials

### 3.3 Band Structures

Since SOC has been reported to have the possibility of influencing the electronic transport in thermoelectrics,<sup>34,93</sup> we computed the electronic structures for GeS, GeSe, SnS, SnSe, SnS<sub>2</sub> and SnSe<sub>2</sub> without and with SOC. The band structures are shown in Figure (3.3). As expected, all materials are found to be semiconductors. The results without and with SOC both show that all materials have indirect band gaps, except for GeSe, which has a direct band gap. The indirect band gap of GeS, SnS, SnSe is between the valence band maxima (VBM) located along the  $\Gamma - X$  path and the conduction band minima (CBM) along the  $Y - \Gamma$  path. For SnS<sub>2</sub> and SnSe<sub>2</sub> the VBM is located along the  $K - M$  path and the CBM at the K-point. For GeSe, the direct band gap is located along the  $\Gamma - X$  path. The band gaps values (with and without SOC) are shown in Table 2. All reference band gaps are from numerical simulation with exception of ref. 69. After applying SOC, we can notice very minor effects on the electronic structure, decreasing slightly the band gaps in all TE materials. The computed band gaps are seen to agree reasonably with the literature values.

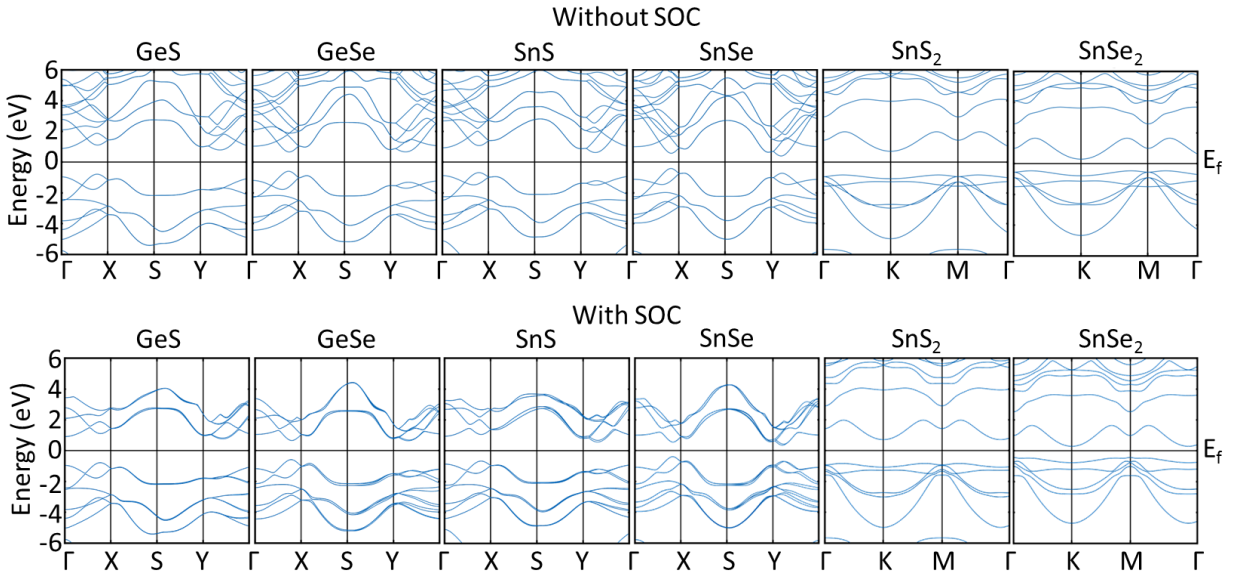


Figure 3.3. Band structures of TE materials (top row) without SOC and (bottom row) with SOC

Table 2. Comparison of band gap energies (eV) with and without SOC for the 2D semiconductors.

Compound	Our values without SOC	Our values with SOC	Literature values without SOC	Reference
	Band Gap (eV)	Band Gap (eV)	Band Gap (eV)	
SnSe	0.83	0.74	1.28	51
			1.12	81
			1.28	87
			0.99	94
			0.77	81
SnS	1.3	1.23	2.57	90
			1.42	94
			1.37	95
GeSe	1.25	1.21	1.16	94
			1.04	95
GeS			1.71	94

	1.58	1.54	1.23	<sup>95</sup>
SnS <sub>2</sub>	1.54	1.50	2.41	<sup>96</sup>
SnSe <sub>2</sub>	0.75	0.73	0.85	<sup>97</sup>
			1.69	<sup>96</sup>

### 3.4 Thermoelectric properties

We compute the TE properties of all materials considering three doping levels corresponding to 300K carrier concentrations of  $10^{18}$ ,  $10^{19}$ , and  $10^{20}$  cm<sup>-3</sup>, respectively. The TE properties are plotted at a temperature range from 300 K to 800 K. The electronic properties of TE materials are influenced by SOC, resulting in some cases with better TE properties such as Seebeck coefficient and electrical conductivity.<sup>36,93,98</sup> Figure (3.4) shows the calculated Seebeck coefficient without and with SOC at different doping levels. The signs of the Seebeck coefficients indicate that SnSe, SnS, SnSe<sub>2</sub> and SnS<sub>2</sub> are n-type, while GeS and GeSe are p-type semiconductors. We can notice that for all cases, the influences of SOC in Seebeck coefficients are small. As a result, for the following text, we use cases without SOC for further study.

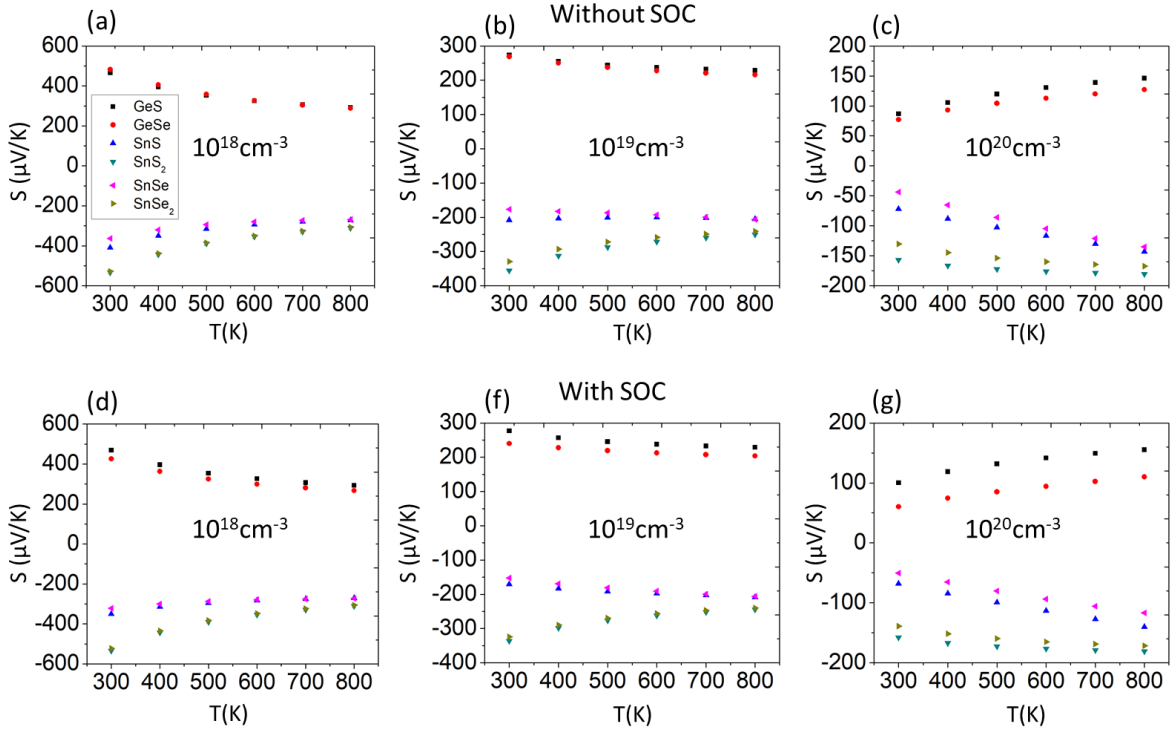


Figure 3.4. Seebeck coefficient as a function of temperature (a-c) without SOC and (d-f) with SOC at different doping levels

Figure (3.5) summarizes all the TE properties without SOC for the materials studied at the three levels of doping. The absolute values of Seebeck coefficients exhibit a decreasing trend with temperature at  $10^{18}$  and  $10^{19} \text{cm}^{-3}$ , with the exception for SnS where the change is small, and for SnSe where the absolute values increase slightly at  $10^{19} \text{cm}^{-3}$ . At  $10^{20}$ , an increasing trend for all TE materials in the Seebeck coefficient in absolute values is observed. Due to the interrelationship between carrier concentration and Seebeck coefficient,<sup>54</sup> we notice that as doping level increases, the Seebeck coefficient decreases dramatically. We can see that for SnS and SnSe, the Seebeck coefficient at 300 K decreases more than 6 times when the doping level increases from  $10^{18} \text{cm}^{-3}$  to  $10^{20} \text{cm}^{-3}$ . As shown in Figure (3.5) (2<sup>nd</sup> row), the electrical conductivity has the same increasing trend for all materials as a function temperature for all three

doping levels. As temperature increase, more electrons are excited and thus the electrical conductivity increases.

After the calculations of the Seebeck coefficient and electrical conductivity, we can calculate the power factor ( $PF = S^2\sigma$ ). The  $PF$  for all compounds at the three doping levels as a function of temperature are shown in Figure (3.5) (3<sup>rd</sup> row). We can notice clearly the temperature dependence of  $PF$ , indicating that as the temperature increases, the  $PF$  for both p- and n-type semiconductors increases monotonically.

The temperature dependence of the electrical thermal conductivity ( $k_e$ ) is shown to be relatively strong (Figures 3.5, 4<sup>th</sup> row). As the temperature increases,  $k_e$  for both p- and n-type semiconductors increases monotonically. In contrast to the  $PF$ , where we seek for a maximum value, for  $k_e$  we want to find a minimum value to maximize  $ZT$ . We can see that the minimum values of  $k_e$  are obtained at  $10^{18} \text{ cm}^{-3}$  level of carrier concentration. GeSe has a minimum value of 0.019 (W/mK) at lower temperature (300 K), and at higher temperature (800 K), GeSe and SnS both have a minimum value of 0.401 (W/m K). To validate and compare our results, we consider the reported experimental values of SnSe, because it is one of the most studied materials due to its high reported thermoelectric properties. From theoretical reports, the number of studies has been consistently increasing in the last decade, and several studies of 2D materials related to this field and presented in this work have been recently reported. For both experimental and theoretical studies, we found a fairly reasonable agreement of electrical properties with our reported values.<sup>48,93,99–105</sup>

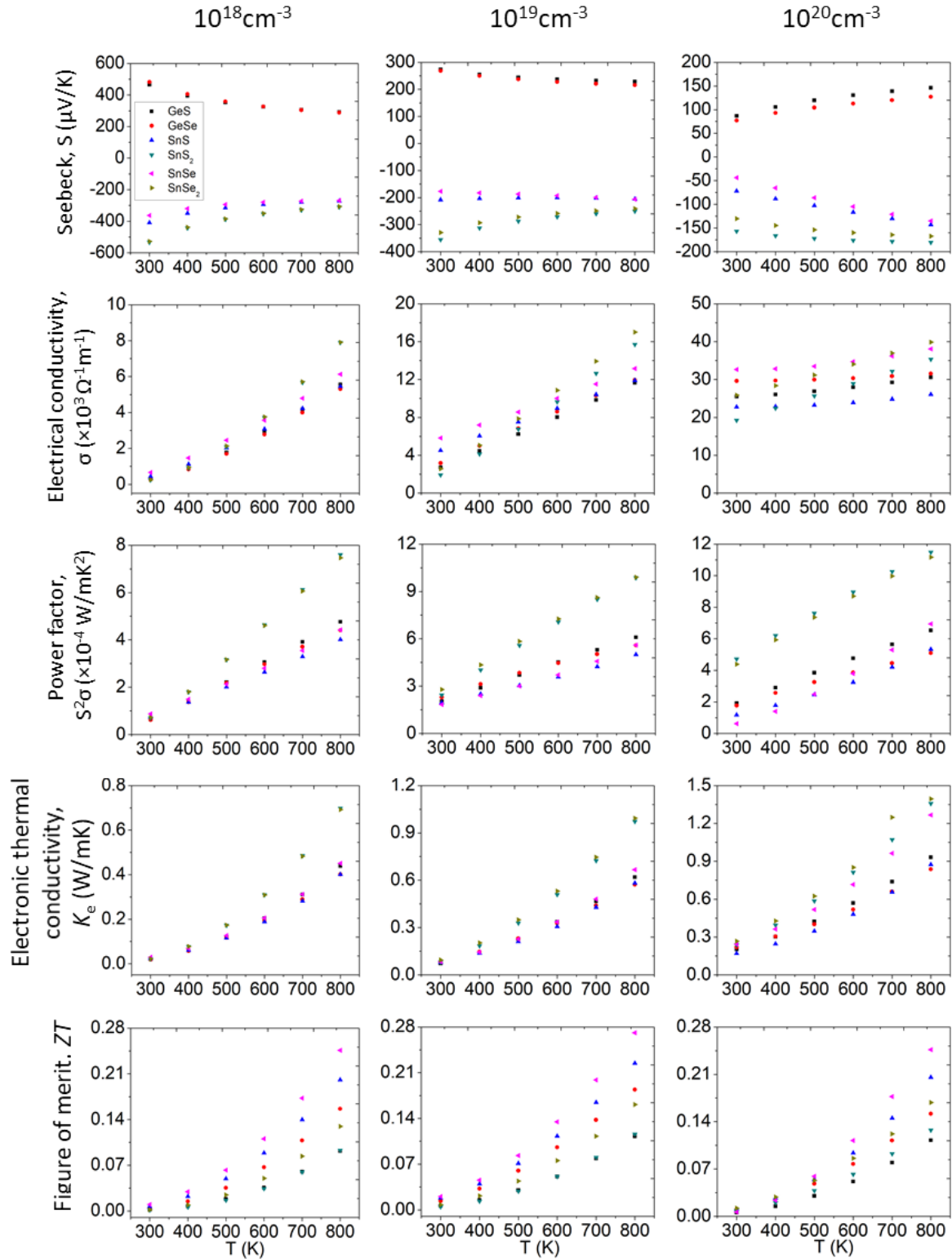


Figure 3.5. TE properties as a function of temperature without SOC at different doping levels

The lattice thermal conductivity, as we mentioned previously, are calculated by solving the Boltzmann transport equation for phonons using the iterative method. The values are shown in Figure (3.6). We can see that as temperature increases, lattice thermal conductivity decreases monotonically. This is because as temperature increases, anharmonic phonon-phonon scattering becomes more intensive, leading to a thermal conductivity inversely proportional to the temperature.<sup>71, 28</sup> The high temperature dependencies are  $\sim T^n$ , where  $n$  is -1.012, -1.003, -0.998, -1.036, -0.999, and -1.015 for GeS, GeSe, SnS, SnS<sub>2</sub>, SnSe, and SnSe<sub>2</sub>, respectively.

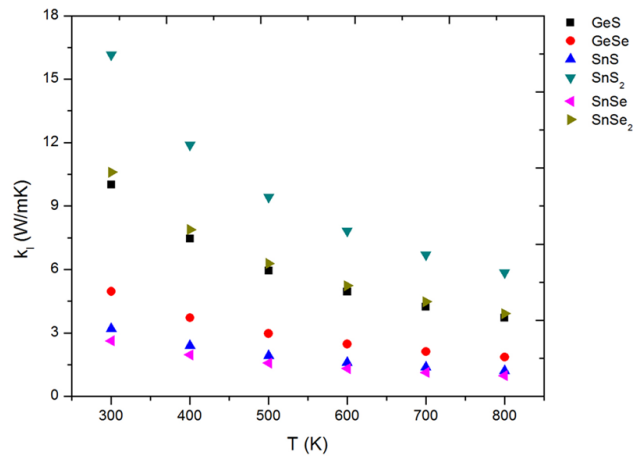


Figure 3.6. Lattice thermal conductivity of 2D TE materials as a function of temperature

All the 2D materials studied here have relatively low lattice thermal conductivity compared with other 2D materials like graphene, MoSe<sub>2</sub>, BN, WS<sub>2</sub>, ZrS<sub>2</sub>, HfS<sub>2</sub>, and ZrSe<sub>2</sub>,<sup>106</sup> making them promising candidates to have higher ZT. The lattice thermal conductivity values obtained in the present work are in good agreement with recently reported results.<sup>104, 107</sup> If we consider the lattice thermal conductivity as a good approach to obtain high efficiency (ZT) in thermoelectric materials, we can expect, from our results (Figure 3.6), that the monolayer SnSe

should be one of the best candidate for thermoelectric applications as we can see in previously reports for this material.<sup>14,19,34,38,43,48,68,84,87,89,101,108–110</sup>

Combining the all the calculated TE properties so far, we obtained the dimensionless figure-of-merit ( $ZT$ ) as a function of temperature for different doping levels (Figure 13, 5<sup>th</sup> row). We notice that the  $ZT$  value can be significantly influenced by temperature. For all materials,  $ZT$  increases with temperature. Among all the 2D materials studied from 300-800K here, the best  $ZT$  values are all obtained from SnSe disregard of doping levels.

## CHAPTER 4: IN-PLANE THERMAL CONDUCTIVITY OF THE NIOBIUM DISELENIDE FROM TEMPERATURE-DEPENDENT RAMAN SPECTROSCOPY

### 4.1 Background

The discovery of graphene<sup>111</sup> and the mechanically ex-foliation technique have led to many advancements in layered materials. Early studies of NbSe<sub>2</sub> demonstrated NbSe<sub>2</sub> to be among the first few layered-structured superconductors with  $T_C$  ranging from 5.9 to 7.0 K. About the same time, bulk thermoelectric properties studies of NbSe<sub>2</sub> showed cross-plane thermal conductivity of 2.1 W/mK. However, despite the electrical properties and the bulk cross-plane thermal conductivity of NbSe<sub>2</sub> have been relatively explored, the in-plane thermal conductivity for thin layer NbSe<sub>2</sub> has remained unknown. In-plane properties are of interest because recent studies on TMDs<sup>112</sup> have shown them to be dissimilar or absent in their bulk form. The main challenge in determining the in-plane thermal conductivity of thin film NbSe<sub>2</sub> lies in the material's tendency of oxidation in ambient environment. However, by utilizing the contactless opto-thermal method we eliminate this concern by enclosing the thin film NbSe<sub>2</sub> sample in vacuum environment.

Temperature-dependent Raman spectroscopy was used previously to determine the thermal conductivity of graphene<sup>113,114</sup> and monolayer MoS<sub>2</sub>.<sup>115</sup> The opto-thermal method extract the  $\kappa$  by the first-order temperature coefficient  $\chi_T$  and power coefficient  $\chi_P$  determined by Raman spectroscopy.<sup>116</sup>

In this work, we performed a thermal transport study using first-principles calculations by DFT and BTE to compute phonon properties including phonon dispersion, group velocity,

scattering phase space, relaxation time, and Gruneisen parameters, that are analyzed to understand the mechanism of thermal conductivity. Thus, the lattice thermal conductivity was computed and compared with the in-plane thermal conductivity obtained from experiments.

## 4.2 Results and discussion

We compute the lattice thermal conductivity of a single layer NbSe<sub>2</sub> using first-principles DFT<sup>117</sup> and the iterative solution to the phonon BTE.<sup>118</sup> The primitive cell of NbSe<sub>2</sub> used in the DFT calculation contains 3 atoms (Figure 4.1). The atomic structure and primitive cell dimension are first optimized using DFT. Then the second order (harmonic) and the third order (anharmonic) force constants are computed using Quantum Espresso<sup>119</sup> together with the density functional perturbation theory (DFPT)<sup>120,121</sup> and finite difference method, respectively.

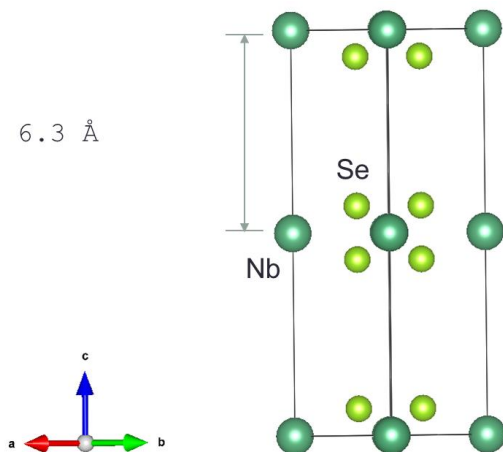


Figure 4. 1. Crystal structures of bulk NbSe<sub>2</sub>. For 2D NbSe<sub>2</sub>, we will only simulate one single molecular layer

We then use the ShengBTE software<sup>64</sup> to solve the linearized phonon BTE iteratively to calculate the thermal conductivity. More details of similar calculations can be found elsewhere.<sup>122</sup> For DFT calculations, the generalized gradient approximation (GGA) of Perdew, Burke, and Ernzerhof (PBE) are used for the exchange-correlation functional. The kinetic energy cutoff of the wave functions is set to 50 Ry for calculations. The Monkhorst-Pack  $k$ -mesh of  $12 \times 12 \times 1$  is used to sample the first Brillouin Zone. Include reference. The convergence for self-consistency (SCF) is set to be  $1.0 \times 10^{-12}$ . We calculate the harmonic force constants using the DFPT as implemented in Quantum Espresso with a  $q$ -point grid size of  $8 \times 8 \times 1$ . Then, a finite difference method based on supercell calculations (cell size of  $5 \times 5 \times 1$ ) is used to extract the cubic force constants. A cutoff radius of 6 Å is used for the third order force constant calculation based on convergence test. These force constants are then fed into the ShengBTE program to calculate thermal conductivity based on an iterative solution of phonon BTE. A  $q$ -mesh of  $30 \times 30 \times 1$  is used for all thermal conductivity calculations. To simulation monolayer, a large vacuum space of at least 10 Å is left in the  $z$ -direction to prevent the interactions between the layer and its periodic images in the cross-plane direction.

For fair comparison with the experimental data,<sup>85</sup> a thickness of 6.3 Å the interlayer distance in bulk NbSe<sub>2</sub>, is used for the single layer NbSe<sub>2</sub> (Figure 4.1). Convergence test of thermal conductivity with respect to the Brillouin zone grid size and third order force constant cutoff has been performed.

The lattice thermal conductivity and cumulative thermal conductivity with respect to mean free path (MFP) of NbSe<sub>2</sub> is shown in Figure 4.2. Convergence tests of thermal conductivity with respect to the Brillouin zone grid size and third order force constants cutoff have been performed. In Figure 4.2(a), we can see that the calculated room temperature lattice

thermal conductivity is  $12.3 \text{ W/mK}$ .

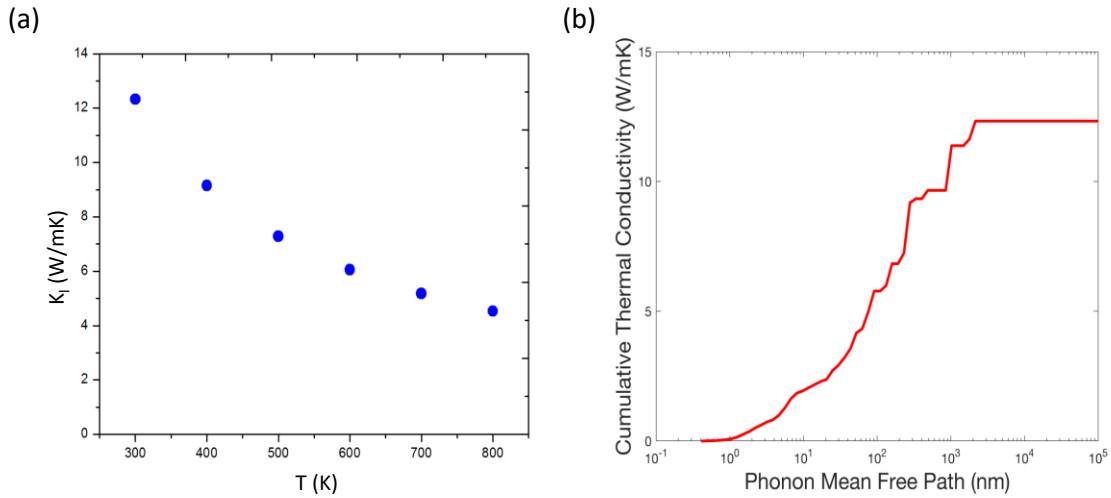


Figure 4. 2. (a) Lattice thermal conductivity and (b) cumulative thermal conductivity of NbSe<sub>2</sub>

The decreasing lattice thermal conductivity of NbSe<sub>2</sub> with increasing temperature is typical of those semiconducting materials (Figure 4.2 a).<sup>123</sup> Lattice thermal conductivity of NbSe<sub>2</sub> decreases with temperature with a scaling relation of  $T^{-1.01}$ . This close to one exponential scaling in high temperature regime indicates the dominating rule of Umklapp type of three-phonon scattering.<sup>71</sup> This low lattice thermal conductivity compared with other 2D materials like graphene, MoS<sub>2</sub>, MoSe<sub>2</sub>, BN, WS<sub>2</sub>, WSe<sub>2</sub>, HfS<sub>2</sub>,<sup>85</sup> making the NbSe<sub>2</sub> as a promising candidates for applications of thermal management in nanoelectronics. On the other hand, the cumulative thermal conductivity at room temperature with respect to MFP is shown in Figure 4.2 (b). The MFP, is a physical property measuring the average distance traveled by a carrier between scattering events and is the product of the magnitude of its velocity and its lifetime. We note that the thermal conductivity is almost exclusively contributed by phonons with MFP greater than 10 nm.

Considering that the experimentally measured thermal conductivity include contributions from both the lattice and electrons, we may extract the electronic thermal conductivity to be  $15.0 - 12.3 = 2.7 \text{ W/mK}$ . If we take the electrical conductivity of bulk NbSe<sub>2</sub> ( $15 \times 10^{-5} \Omega \cdot \text{cm}$ ) from the literature and calculate the corresponding electronic thermal conductivity using Widemann-Franz law, a value of  $4.9 \text{ W/mK}$  is obtained. Considering the uncertain in the experimental measurement and quality of the sample, we deem the agreement between the calculations and experiments quite well. Moreover, in the experiment, samples of thicknesses of 20, 25 and 120 nm were studied. These samples may consist of 32 layers or more of NbSe<sub>2</sub>, which should be thick enough to avoid any thickness effect. Studies have shown that from single layer to bulk MoS<sub>2</sub>, a material similar to NbSe<sub>2</sub> in structure and interlayer bonding, the thermal conductivity reduces by  $\sim 30\%$ .<sup>124</sup> If we consider a similar reduction ratio for NbSe<sub>2</sub>, the lattice thermal conductivity of bulk NbSe<sub>2</sub> would be  $8.6 \text{ W/mK}$ . Summing it up with the electronic thermal conductivity from the Widemann-Franz law, a total thermal conductivity of  $13.5 \text{ W/mK}$  is obtained, which is still well within the uncertainty of the experimental result of  $k = 14 \pm 5 \text{ W/mK}$ .

To understand the thermal transport behavior, we analyze the phonon properties: phonon dispersion, group velocity, relaxation time, scattering phase space, and Gruneisen parameters, which influence the lattice thermal conductivity. We first visualize the phonon dispersion of NbSe<sub>2</sub> (Figure 4.3) along the high symmetric lines in the first Brillouin zone. We can observe that the acoustic modes are the dominant contributors to the thermal conductivity, and the quadratic flexural ZA modes are common among 2D materials.<sup>106,116,122,125,126</sup>

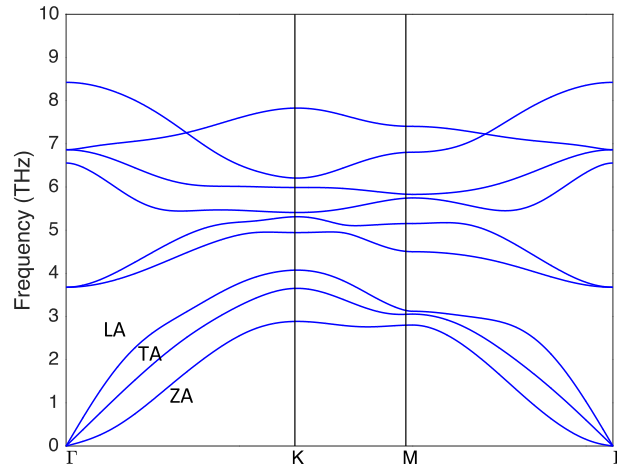


Figure 4. 3. Phonon dispersion of NbSe<sub>2</sub>

For all the three acoustic modes near the  $\Gamma$  point, we can observe slightly higher group velocity for NbSe<sub>2</sub>. Detailed group velocity profile as a function of phonon frequency is shown in Figure 4.4(a). We can notice that the phonon group velocity is dominant at low frequencies (< 4 THz).

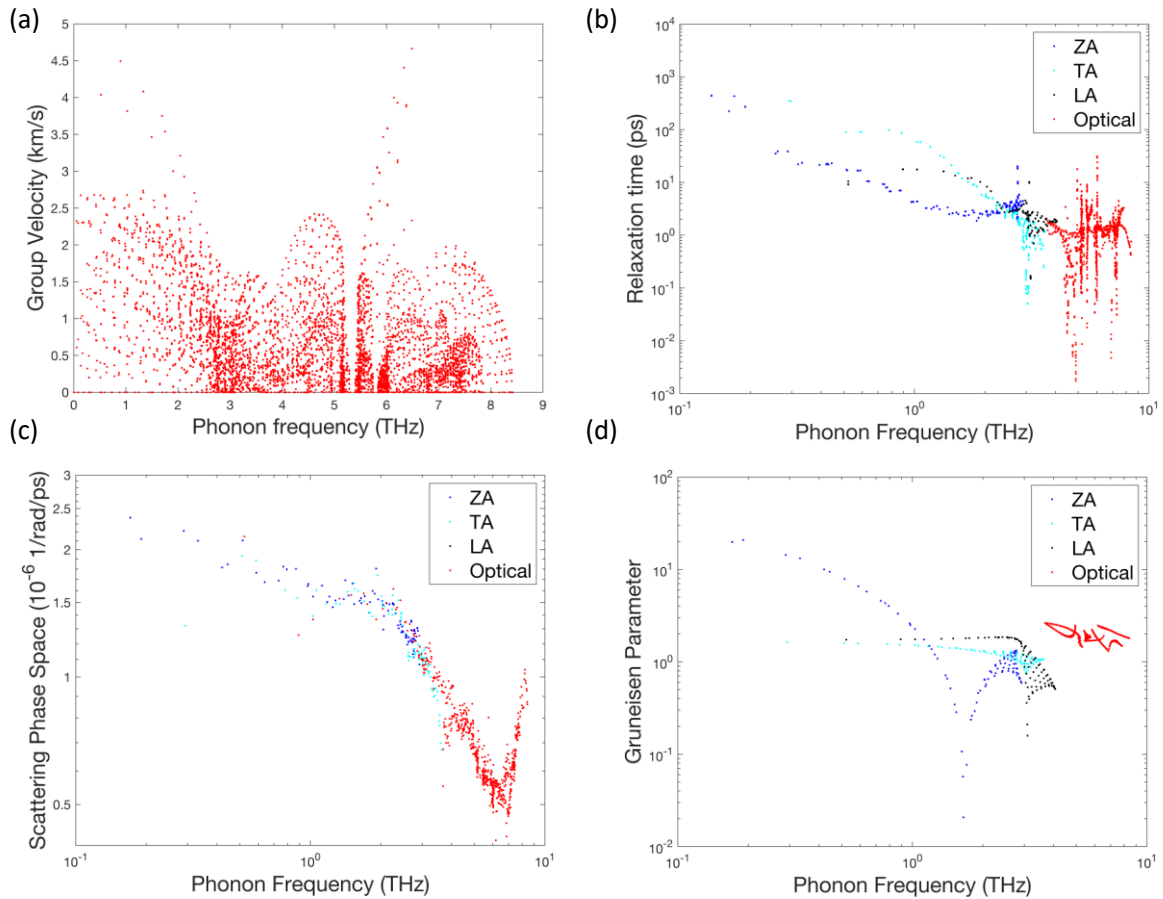


Figure 4. 4. (a) Phonon group velocity, (b) relaxation times, (c) scattering phase space, and (d) Gruneisen parameter of NbSe<sub>2</sub>

One interesting thing is the contribution of thermal conductivity from each polarization. ZA, TA, and LA modes contribute to the thermal conductivity with 2.80 W/mK, 6.74 W/mK, and 2.24 W/mK, respectively, and optical modes combined contribute with only 0.48 W/mK. It is clear that in NbSe<sub>2</sub>, TA mode dominates the heat transport. The Figure 4.4(b) shows the relaxation time as a functional of phonon frequency. We can see that the TA modes do have orders of magnitude larger relaxation time than ZA and LA modes. This larger phonon lifetime is thus the reason of the prime position of TA mode. In three-phonon scattering process, there are two main aspects determining the phonon lifetime. One is the number of possible scattering

channels and the other is the strength of the scattering. The number of possible scattering channels can be quantified as the three-phonon scattering phase space, which counts the number of possible scattering channels for all phonon polarizations in first Brillouin zone where energy and quasi-momentum conservation is satisfied.<sup>127</sup> The larger phase space is, the more possible this phonon mode can be scattered in either absorption or emission. The other is the strength of three-phonon scattering. Gruneisen parameter is a dimensionless physical parameter describing the anharmonicity of the materials for each phonon modes and thus describing the strength of three-phonon scattering.<sup>14</sup> Larger Gruneisen parameter means larger anharmonicity, leading to stronger scattering and smaller thermal conductivity. It can be seen in Figure 4.4(c) that the three acoustic modes do not differ significantly. On the other hand, a clear difference of Gruneisen parameter for these three acoustic phonon modes can be seen in Figure 4.4(d). In long wave limit, the main contributor for thermal conductivity, ZA mode does have a much larger anharmonicity and this clear difference in Gruneisen parameter is no doubt the main reason for the different roles in acoustic phonon modes. The deeper physical nature of why the transverse mode has smaller anharmonicity is not clear but this interesting finding may help us understand more of phonon transport in this kind of monolayer materials.

## CHAPTER 5: CONCLUSIONS AND FUTURE WORK

### 5.1. Conclusions

This thesis contributes, specifically, to the understanding the transport properties and its interactions occurring in metal and thermoelectric materials. The central goal of this thesis consists of an understanding of electron and phonon transport, in particular their interaction to compute electronic and thermal properties in bulk and monolayer compounds.

In Chapter 2, the electronic transport properties behavior of un-doped cold-pressed SnSe was determined upon annealing cycles from RT to 800 K revealing, in particular, a significant improvement of the Seebeck coefficient and, therefore, the Power Factor. On the other hand, the XRD data revealed a texture or preferred orientation of the grains after annealing processes. The lattice thermal conductivity of the studied sample in the temperature range of 300 to 800 K showed a similar behavior than the reported ones for other un-doped polycrystalline SnSe, with a scaling relation value of  $T^{-0.577}$ . Finally, the figure of merit,  $ZT$ , reaches a value of 0.11 at 772 K.

In Chapter 3, DFT and the Boltzmann transport model are used to calculate the TE properties of monolayer materials belonging to the group IV-VI compounds, including SnSe, GeSe, SnS, GeS, SnSe<sub>2</sub> and SnS<sub>2</sub>. We determine the electronic bands and Seebeck coefficient without and with SOC. We notice a small effect of SOC over the band gaps for all materials. Indirect band gaps from calculations without SOC of 0.83 eV, 1.3 eV, 1.58 eV, 0.75 eV, and 1.54 eV are obtained for SnSe, SnS, GeS, SnSe<sub>2</sub> and SnS<sub>2</sub>, respectively. A direct band gaps of 1.25 eV is found for GeSe. We also obtain indirect band gaps from calculations with SOC of 0.74 eV, 1.23 eV, 1.54 eV, 0.73 eV, and 1.5 eV for SnSe, SnS, GeS, SnSe<sub>2</sub> and SnS<sub>2</sub>, respectively, and a direct band gap of 1.21 eV for GeSe. The TE properties are calculated at

different doping levels, and it was found that SnSe has the largest ZT disregard the doping level, which is related to the low lattice thermal conductivity of this material.

Finally, in Chapter 4, we report the thermal transport study, where the phonon properties and lattice thermal conductivity were computed. We used first-principles calculations by DFT and BTE to compute the phonon properties and lattice thermal conductivity of thin film NbSe<sub>2</sub>. We found that our estimation of thermal conductivity of 13.5 W/mK, are in good agreement with the in-plane thermal conductivity obtained from experiments, where the thermal conductivity reaches  $14 \pm 5$  W/mK at room temperature. On the other hand, one interesting thing is the contribution of thermal conductivity from each polarization. ZA, TA, and LA modes contribute to the thermal conductivity with 2.80 W/mK, 6.74 W/mK, and 2.24 W/mK, respectively, and optical modes combined contribute with only 0.48 W/mK. It is clear that in NbSe<sub>2</sub>, TA mode dominates the heat transport.

## 5.2. Future Work

Whereas the aim of this thesis was to investigate the structural and morphological behavior of bulk material through characterization techniques, and determine the electronic and thermal properties using both experimental and simulation methods, I would like to continue along this path to explore the electronic and thermal properties of new compounds and material families. Since the experimental research showed in this thesis is interesting, I want to attain a deep understanding of heat transfer mechanism in materials. To accomplish this, I would like to explore and investigate by experimental methods from different techniques, the methodology to measure the phonon transport in materials. In addition, I want to continue learn simulation methods, using first principles by DFT and DFPT, and BTE, for calculations with more details the electronic and thermal properties on interesting materials such as new families of 2D

materials, VO<sub>2</sub>, Mo<sub>2</sub>C, MoC, and topological TE materials. I believe my future research will lead me to learn and understand the transport and interaction of electrons and phonons, and hopefully these understanding will eventually contribute to innovative material science, designing new materials and applying novel methods in engineering.

## References

1. Ioffe, A. F. *Semiconductor thermoelements, and thermoelectric cooling*. (Infosearch, 1957).
2. J.R. Sootsman, D.Y. Chung, M. G. K. New and old concepts in thermoelectric materials. *Angew. Chemie, Int. Ed.* **48**, 8616–8639 (2009).
3. C.J. Vineis, A. Shakouri, A. Majumdar, M. G. K. Nanostructured thermoelectrics: big efficiency gains from small features. *Adv. Mater.* **22**, 3970–3980 (2010).
4. Barma, M. C., Riaz, M., Saidur, R. & Long, B. D. Estimation of thermoelectric power generation by recovering waste heat from Biomass fired thermal oil heater. *Energy Convers. Manag.* **98**, 303–313 (2015).
5. Favarel, C., Bédécarrats, J.-P., Kousksou, T. & Champier, D. Experimental analysis with numerical comparison for different thermoelectric generators configurations. *Energy Convers. Manag.* **107**, 114–122 (2015).
6. Moraes, F. S. *et al.* Solar thermoelectric generator performance relative to air speed. *Energy Convers. Manag.* **99**, 326–333 (2015).
7. Kraemer, D. *et al.* High-performance flat-panel solar thermoelectric generators with high thermal concentration. *Nat. Mater.* **10**, 532–538 (2011).
8. Brown, S. R., Kauzlarich, S. M., Gascoin, F. & Snyder, G. J. Yb<sub>14</sub>MnSb<sub>11</sub>: New High Efficiency Thermoelectric Material for Power Generation. *Chem. Mater.* **18**, 1873–1877 (2006).
9. Funahashi, R. & Shikano, M. Bi<sub>2</sub>Sr<sub>2</sub>Co<sub>2</sub>O<sub>y</sub> whiskers with high thermoelectric figure of merit. *Appl. Phys. Lett.* **81**, 1459–1461 (2002).
10. Zebarjadi, M., Esfarjani, K., Dresselhaus, M. S., Ren, Z. F. & Chen, G. Perspectives on thermoelectrics: from fundamentals to device applications. *Energy Environ. Sci.* **5**, 5147–5162 (2012).
11. Biswas, K. *et al.* High-performance bulk thermoelectrics with all-scale hierarchical architectures. *Nature* **489**, 414–8 (2012).
12. Pei, Y. *et al.* Convergence of electronic bands for high performance bulk thermoelectrics. *Nature* **473**, 66–69 (2011).
13. Heremans, J. P. *et al.* Enhancement of thermoelectric efficiency in PbTe by distortion of the electronic density of states. *Science (80- )*. **321**, 554–557 (2008).
14. Zhao, L.-D. *et al.* Ultralow thermal conductivity and high thermoelectric figure of merit in SnSe crystals. *Nature* **508**, 373–7 (2014).
15. Zhao, L.-D. *et al.* Ultrahigh power factor and thermoelectric performance in hole-doped single-crystal SnSe. *Science (80- )*. **351**, (2016).
16. Chen, C.-L., Wang, H., Chen, Y.-Y., Day, T. & Snyder, J. Thermoelectric properties of p-type polycrystalline SnSe doped with Ag. *J. Mater. Chem. A* **2**, 11171–11176 (2014).

17. Li, Y., Shi, X., Ren, D., Chen, J. & Chen, L. Investigation of the anisotropic thermoelectric properties of oriented polycrystalline SnSe. *Energies* **8**, 6275–6285 (2015).
18. Zhang, Q. *et al.* Studies on Thermoelectric Properties of n-type Polycrystalline SnSe 1- x S x by Iodine Doping. 1–8 (2015). doi:10.1002/aenm.201500360
19. Leng, H.-Q., Zhou, M., Zhao, J., Han, Y.-M. & Li, L.-F. The thermoelectric performance of anisotropic SnSe doped with Na. *RSC Adv.* **6**, 9112–9116 (2016).
20. Han, Y.-M. *et al.* Thermoelectric performance of SnS and SnS–SnSe solid solution. *J. Mater. Chem. A* **3**, 4555–4559 (2015).
21. Minnich, a J., Dresselhaus, M. S., Ren, Z. F. & Chen, G. Bulk nanostructured thermoelectric materials: current research and future prospects. *Energy Env. Sci* **2**, 466–479 (2009).
22. Joshi, G. *et al.* Enhanced thermoelectric figure-of-merit in nanostructured p-type silicon germanium bulk alloys. *Nano Lett.* **8**, 4670–4674 (2008).
23. Sootsman JR, Kong H, Uher C, D’Angelo JJ, Wu CI, Hogan TP, Caillat T, K. M. Large enhancements in the thermoelectric power factor of bulk PbTe at high temperature by synergistic nanostructuring. *Angew Chem Int Ed Engl* **47**, 8618–22 (2008).
24. Zhang, Q. *et al.* High thermoelectric performance by resonant dopant indium in nanostructured SnTe. *Proc. Natl. Acad. Sci. U. S. A.* **110**, 13261–6 (2013).
25. Heremans, J. P., Wiendlocha, B. & Chamoire, A. M. Resonant levels in bulk thermoelectric semiconductors. *Energy Environ. Sci.* **5**, 5510–5530 (2012).
26. Jaworski, C. M., Wiendlocha, B., Jovovic, V. & Heremans, J. P. Combining alloy scattering of phonons and resonant electronic levels to reach a high thermoelectric figure of merit in PbTeSe and PbTeS alloys. *Energy Environ. Sci.* **4**, 4155 (2011).
27. Girard, S. N. *et al.* High performance Na-doped PbTe-PbS thermoelectric materials: Electronic density of states modification and shape-controlled nanostructures. *J. Am. Chem. Soc.* **133**, 16588–16597 (2011).
28. Balandin, A. & Wang, K. L. Effect of phonon confinement on the thermoelectric figure of merit of quantum wells. *J. Appl. Phys.* **84**, 6149 (1998).
29. Leonov, V. & Vullers, R. J. M. Wearable thermoelectric generators for body-powered devices. *J. Electron. Mater.* **38**, 1491–1498 (2009).
30. Li, H.-M. *et al.* Metal-semiconductor Li barrier modulation for high photoresponse in transition metal dichalcogenide field effect transistors. *Sci. Rep.* **4**, 4041 (2014).
31. Geim, A. K. & Novoselov, K. S. The rise of graphene. *Nat. Mater.* **6**, 183–91 (2007).
32. Geim, A. K. Graphene : Status and Prospects. **1530**, (2010).
33. Gu, X. K. & Yang, R. G. Phonon transport in single-layer transition metal dichalcogenides: A first-principles study. *Appl. Phys. Lett.* **105**, 5 (2014).
34. Guan, X. *et al.* Thermoelectric properties of SnSe compound. *J. Alloys Compd.* **643**, 116–

- 120 (2015).
35. Guo, R., Wang, X., Kuang, Y. & Huang, B. First-principles study of anisotropic thermoelectric transport properties of IV-VI semiconductor compounds SnSe and SnS. *Phys. Rev. B - Condens. Matter Mater. Phys.* **92**, 1–13 (2015).
  36. Guo, S.-D. Strain effect on power factor in monolayer MoS<sub>2</sub>. *Comput. Mater. Sci.* **123**, 8–13 (2016).
  37. Guo, S. Thermoelectric properties of orthorhombic group IV-VI monolayers from the first-principles calculations. *Appl. Phys. Lett* **121**, 1–7 (2017).
  38. Hong, a. J. *et al.* Optimizing the thermoelectric performance of low-temperature SnSe compounds by electronic structure design. *J. Mater. Chem. A* **3**, 13365–13370 (2015).
  39. Jin, Z. *et al.* A Revisit to High Thermoelectric Performance of Single-layer MoS<sub>2</sub>. *Sci. Rep.* **5**, 18342 (2015).
  40. Khan, A. A., Khan, I., Ahmad, I. & Ali, Z. Thermoelectric studies of IV-VI semiconductors for renewable energy resources. *Mater. Sci. Semicond. Process.* **48**, 85–94 (2016).
  41. Kim, J. Y. & Grossman, J. C. High-efficiency thermoelectrics with functionalized graphene. *Nano Lett.* **15**, 2830–2835 (2015).
  42. Kumar, S. & Schwingenschl??gl, U. Thermoelectric response of bulk and monolayer MoSe<sub>2</sub> and WSe<sub>2</sub>. *Chem. Mater.* **27**, 1278–1284 (2015).
  43. Kutorasinski, K., Wiendlocha, B., Kaprzyk, S. & Tobola, J. Electronic structure and thermoelectric properties of n - and p -type SnSe from first-principles calculations. *Phys. Rev. B* **91**, 205201 (2015).
  44. Larentis, S., Fallahazad, B. & Tutuc, E. Field-effect transistors and intrinsic mobility in ultra-thin MoSe<sub>2</sub> layers. *Appl. Phys. Lett.* **101**, 1–4 (2012).
  45. Kim, S. J., We, J. H. & Cho, B. J. A wearable thermoelectric generator fabricated on a glass fabric. *Energy Environ. Sci.* **7**, 1959 (2014).
  46. Bahk, J.-H., Fang, H., Yazawa, K. & Shakouri, A. Flexible thermoelectric materials and device optimization for wearable energy harvesting. *J. Mater. Chem. C* **3**, 10362–10374 (2015).
  47. Zhang, G. & Zhang, Y.-W. Thermoelectric properties of two-dimensional transition metal dichalcogenides. *J. Mater. Chem. C* **5**, 7684–7698 (2017).
  48. Li, G., Ding, G. & Gao, G. Thermoelectric properties of SnSe<sub>2</sub> monolayer. *J. Phys. Condens. Matter* **29**, 015001 (2017).
  49. Nolas, G.S., Sharp, J., Goldsmid, J. *Thermoelectrics Basic Principles and New Materials Developments.* (Springer Series in Materials Science, 2001).
  50. Rowe, D. M. *Handbook of Thermoelectric Materials.* (1995).
  51. Butt, F. K. *et al.* Synthesis of highly pure single crystalline SnSe nanostructures by

- thermal evaporation and condensation route. *Mater. Chem. Phys.* **137**, 565–570 (2012).
52. Levi, B. G. Simple compound manifests record-high thermoelectric performance. *Phys. Today* **67**, 14–16 (2014).
  53. Hamid Elsheikh, M. *et al.* A review on thermoelectric renewable energy: Principle parameters that affect their performance. *Renew. Sustain. Energy Rev.* **30**, 337–355 (2014).
  54. Snyder, G. J. & Toberer, E. S. Complex thermoelectric materials. *Nat. Mater.* **7**, 105–114 (2008).
  55. Kohn, W. & Sham, L. J. Self-Consistent Equations Including Exchange and Correlation Effects. *Phys. Rev.* **140**, A1134–A1138 (1965).
  56. Feliciano Giustino. *Materials Modeling Using Density Functional Theory*. (Oxford University Press, Inc., 2014).
  57. Madsen, G. K. H. & Singh, D. J. BoltzTraP. A code for calculating band-structure dependent quantities. *Comput. Phys. Commun.* **175**, 67–71 (2006).
  58. Clark, G. L. & Duane, W. The abnormal reflection of X-rays by crystals. *Science (80- )*. **58**, 400–402 (1923).
  59. Sowinska, M. In-operando hard X-ray photoelectron spectroscopy study on the resistive switching physics of HfO<sub>2</sub>-based RRAM. (2014).
  60. Das, R. S. & Agrawal, Y. K. Raman spectroscopy: Recent advancements, techniques and applications. *Vib. Spectrosc.* **57**, 163–176 (2011).
  61. Ludemann, M. *et al.* Raman spectroscopy insights into the size-induced structural transformation in sncs nanolayers. *Langmuir* **30**, 8209–8214 (2014).
  62. Bumbrah, G. S. & Sharma, R. M. Raman spectroscopy – Basic principle, instrumentation and selected applications for the characterization of drugs of abuse. *Egypt. J. Forensic Sci.* **6**, 209–215 (2016).
  63. Giannozzi, P. *et al.* QUANTUM ESPRESSO: a modular and open-source software project for quantum simulations of materials. *J. Phys. Condens. Matter* **21**, 395502 (2009).
  64. Li, W., Carrete, J., Katcho, N. A. & Mingo, N. ShengBTE: A solver of the Boltzmann transport equation for phonons. *Comput. Phys. Commun.* **185**, 1747–1758 (2014).
  65. Jarabek, B. R. *et al.* XRD and TEM Characterization of Compound Semiconductor Solid Solutions: Sn(S,Se) and (Pb,Cd)S. *JCPDS-International Cent. Diffraction Data* (1997).
  66. Parker, W. J., Jenkins, R. J., Butler, C. P. & Abbott, G. L. Flash method of determining thermal diffusivity, heat capacity, and thermal conductivity. *J. Appl. Phys.* **32**, 1679–1684 (1961).
  67. Fu, Y. *et al.* Enhanced thermoelectric performance in p-type polycrystalline SnSe benefiting from texture modulation. *J. Mater. Chem. C* (2016). doi:10.1039/C5TC03652F
  68. Chere, E. K. *et al.* Studies on thermoelectric figure of merit of Na-doped p-type polycrystalline SnSe. *J. Mater. Chem. A* **4**, 1848–1854 (2016).

69. Sassi, S. *et al.* Assessment of the thermoelectric performance of polycrystalline p -type SnSe. *Appl. Phys. Lett.* **104**, (2014).
70. Jiang, J., Li, Y., Xu, G., Cui, P. & Chen, L. Effect of annealing treatment on thermoelectric properties of n-type Bi-Te-Se sintered materials. in 64–66 (Thermoelectrics, 2007. ICT 2007. 26th International Conference on, 2007). doi:10.1109/ICT.2007.4569424
71. Gang Chen. *NANOSCALE ENERGY TRANSPORT AND CONVERSION*. (Oxford University Press, Inc., 2005).
72. Swartz, E. T. & Pohl, R. O. Thermal boundary resistance. *Rev. Mod. Phys.* **61**, 605–668 (1989).
73. Wu, X. & Luo, T. The importance of anharmonicity in thermal transport across solid-solid interfaces. *J. Appl. Phys.* **115**, (2014).
74. Zhou, J., Liao, B. & Chen, G. First-principles calculations of thermal, electrical, and thermoelectric transport properties of semiconductors. *Semicond. Sci. Technol.* **31**, 043001 (2016).
75. Giannozzi, P. *et al.* QUANTUM ESPRESSO: a modular and open-source software project for quantum simulations of materials. *J. Phys. Condens. Matter* **21**, 395502 (2009).
76. Perdew, J. P., Burke, K. & Ernzerhof, M. Generalized Gradient Approximation Made Simple. *Phys. Rev. Lett.* **77**, 3865–3868 (1996).
77. Khan, A. A., Khan, I., Ahmad, I. & Ali, Z. Thermoelectric studies of IV-VI semiconductors for renewable energy resources. *Mater. Sci. Semicond. Process.* **48**, 85–94 (2016).
78. Singh, A. K. & Hennig, R. G. Computational prediction of two-dimensional group-IV mono-chalcogenides Computational prediction of two-dimensional group-IV mono-chalcogenides. *Appl. Phys. Lett.* **042103**, (2016).
79. Fei, R., Li, W., Li, J. & Yang, L. Giant piezoelectricity of monolayer group IV monochalcogenides: SnSe, SnS, GeSe, and GeS. *Appl. Phys. Lett.* **107**, (2015).
80. Løvvik, O. M. & Prytz. Density-functional band-structure calculations for La-, Y-, and Sc-filled CoP3-based skutterudite structures. *Phys. Rev. B - Condens. Matter Mater. Phys.* **70**, 1–6 (2004).
81. Ding, G., Gao, G. & Yao, K. High-efficient thermoelectric materials: The case of orthorhombic IV-VI compounds. *Sci. Rep.* **5**, 9567 (2015).
82. Yabuuchi, S., Okamoto, M., Nishide, A., Kurosaki, Y. & Hayakawa, J. Large Seebeck Coefficients of Fe<sub>2</sub>TiSn and Fe<sub>2</sub>TiSi: First-Principles Study. *Appl. Phys. Express* **6**, 025504 (2013).
83. Gao, X. *et al.* Theoretical studies on the thermopower of semiconductors and low-band-gap crystalline polymers. *Phys. Rev. B - Condens. Matter Mater. Phys.* **72**, 1–7 (2005).
84. Carrete, J., Mingo, N., Curtarolo, S., Mingo, N. & Curtarolo, S. Low thermal conductivity and triaxial phononic anisotropy of SnSe Low thermal conductivity and triaxial phononic

- anisotropy of SnSe. *Appl. Phys. Lett.* **101907**, 1–5 (2014).
85. Wu, X. *et al.* How to characterize thermal transport capability of 2D materials fairly?- Sheet thermal conductance and the choice of thickness. *Chem. Phys. Lett.* **669**, 233–237 (2017).
  86. Liu, Z., Wu, X. & Luo, T. The impact of hydrogenation on the thermal transport of silicene. *2D Mater.* **4**, 025002 (2017).
  87. Wang, F. Q., Zhang, S., Yu, J. & Wang, Q. Thermoelectric properties of single-layered SnSe sheet. *Nanoscale* **7**, 15962–15970 (2015).
  88. Sun, B.-Z., Ma, Z., He, C. & Wu, K. Anisotropic thermoelectric properties of layered compounds in SnX<sub>2</sub> (X = S, Se): a promising thermoelectric material. *Phys. Chem. Chem. Phys.* **17**, 29844–29853 (2015).
  89. Guo, R., Wang, X., Kuang, Y. & Huang, B. First-principles study of anisotropic thermoelectric transport properties of IV-VI semiconductor compounds SnSe and SnS. *Phys. Rev. B - Condens. Matter Mater. Phys.* **92**, 1–42 (2015).
  90. Tritsarlis, G. A., Malone, B. D. & Kaxiras, E. Optoelectronic properties of single-layer, double-layer, and bulk tin sulfide: A theoretical study. *J. Appl. Phys.* **113**, (2013).
  91. Sava, F. *et al.* Amorphous SnSe<sub>2</sub> films. *J. Optoelectron. Adv. Mater.* **8**, 1367–1371 (2006).
  92. Bauer Pereira, P. *et al.* Lattice dynamics and structure of GeTe, SnTe and PbTe. *J. Appl. Phys.* **8**, 1300–1307 (2013).
  93. Guo, S. D. & Wang, Y. H. Thermoelectric properties of orthorhombic group IV-VI monolayers from the first-principles calculations. *J. Appl. Phys.* **121**, 0–7 (2017).
  94. Shafique, A. & Shin, Y. Thermoelectric and phonon transport properties of two-dimensional IV – VI compounds. *Sci. Rep.* **7**, 1–10 (2017).
  95. Fei, R., Li, W., Li, J., and Yang, L. Giant Piezoelectric in Monolayer Group IV Monochalcogenides SnSe, SnS, GeSe. *J. Chem. Inf. Model.* **107**, (2015).
  96. Gonzalez, J. M. & Oleynik, I. I. Layer-dependent properties of SnS<sub>2</sub> and SnSe<sub>2</sub> novel two-dimensional materials. doi:10.1103/PhysRevB.94.125443
  97. Li, G., Ding, G. & Gao, G. Thermoelectric properties of SnSe<sub>2</sub> monolayer. *J. Phys. Condens. Matter* **29**, 015001 (2017).
  98. Guo, S.-D. & Zhang, L. Biaxial strain tuned thermoelectric properties in monolayer  $\text{PtSe}_2$ . *J. Mater. Chem. C* **4**, 9366–9374 (2016).
  99. Kumar, S. & Schwingenschlögl, U. Thermoelectric response of bulk and monolayer MoSe<sub>2</sub> and WSe<sub>2</sub>. *Chem. Mater.* **27**, 1278–1284 (2015).
  100. Sun, B.-Z., Ma, Z., He, C. & Wu, K. Anisotropic thermoelectric properties of layered compounds in SnX<sub>2</sub> (X = S, Se): a promising thermoelectric material. *Phys. Chem. Chem. Phys.* **17**, 29844–29853 (2015).

101. Morales Ferreiro, J. O. *et al.* Effect of the annealing on the power factor of un-doped cold-pressed SnSe. *Appl. Therm. Eng.* (2016). doi:10.1016/j.applthermaleng.2016.07.198
102. Zhang, Q. *et al.* Studies on Thermoelectric Properties of n-type Polycrystalline SnSe<sub>1-x</sub>S<sub>x</sub> by Iodine Doping. *Adv. Energy Mater.* **5**, 1–8 (2015).
103. Tyagi, K. *et al.* Electrical transport and mechanical properties of thermoelectric tin selenide. *RSC Adv.* **6**, 11562–11569 (2016).
104. Shafique, A. & Shin, Y. Thermoelectric and phonon transport properties of two-dimensional IV – VI compounds. *Sci. Rep.* **7**, 1–10 (2017).
105. Ding, Y., Xiao, B., Tang, G. & Hong, J. Transport Properties and High Thermopower of SnSe<sub>2</sub>: A Full Ab-Initio Investigation. *J. Phys. Chem. C* **121**, 225–236 (2017).
106. Wu, X. *et al.* How to Characterize Thermal Transport Capability of 2D Materials Fairly? - Sheet Thermal Conductance and the Choice of Thickness. *arXiv* **7**, 06542 (2016).
107. Qin, G., Qin, Z., Fang, W. & Zhang, L. Diverse anisotropy of phonon transport in two-dimensional group IV-VI compounds: A comparative study. *Nanoscale* **8**, 11306–11319 (2016).
108. Zhao, L. *et al.* Ultrahigh power factor and thermoelectric performance in hole-doped single-crystal SnSe. **2**, 1–7 (2015).
109. Popuri, S. R. *et al.* Large thermoelectric power factors and impact of texturing on the thermal conductivity in polycrystalline SnSe. *J. Mater. Chem. C* **4**, 1685–1691 (2016).
110. Sassi, S. *et al.* Transport Properties of Polycrystalline p-type SnSe. *Mater. Today Proc.* **2**, 690–698 (2015).
111. Novoselov, K. S. *et al.* Two-dimensional gas of massless Dirac fermions in graphene. *Nature* **438**, 197–200 (2005).
112. Wang, Q. H., Kalantar-zadeh, K., Kis, A., Coleman, J. N. & Strano, M. S. transition metal dichalcogenides. *Nat. Publ. Gr.* **7**, 699–712 (2012).
113. Balandin, A. A. *et al.* Superior thermal conductivity of single-layer graphene. *Nano Lett.* **8**, 902–907 (2008).
114. Cai, W. *et al.* Thermal transport in suspended and supported monolayer graphene grown by chemical vapor deposition. *Nano Lett.* **10**, 1645–1651 (2010).
115. Yan, R. *et al.* Thermal conductivity of monolayer molybdenum disulfide obtained from temperature-dependent Raman spectroscopy. *ACS Nano* **8**, 986–993 (2014).
116. Judek, J. *et al.* High accuracy determination of the thermal properties of supported 2D materials. *Sci. Rep.* **5**, 12422 (2015).
117. Zhou, J., Liao, B. & Chen, G. First-principles calculations of thermal, electrical, and thermoelectric transport properties of semiconductors. *Semicond. Sci. Technol.* **31**, 043001 (2016).
118. Broido, D. A., Malorny, M., Birner, G., Mingo, N. & Stewart, D. A. Intrinsic lattice

- thermal conductivity of semiconductors from first principles. *Appl. Phys. Lett.* **91**, (2007).
119. Gulans, A. *et al.* project QUANTUM ESPRESSO : a modular and open-source software project for quantum simulations of materials. doi:10.1088/0953-8984/21/39/395502
  120. Gonze, X. & Lee, C. Dynamical matrices, Born effective charges, dielectric permittivity tensors, and interatomic force constants from density-functional perturbation theory. *Phys. Rev. B* **55**, 10355–10367 (1997).
  121. Baroni, S. *et al.* Phonons and related crystal properties from density-functional perturbation theory. *Rev. Mod. Phys.* **73**, (2001).
  122. Liu, Z., Wu, X. & Luo, T. The impact of hydrogenation on the thermal transport of silicene. *2D Mater.* **4**, 025002 (2017).
  123. Jain, A. & McGaughey, A. J. H. Thermal transport by phonons and electrons in aluminum, silver, and gold from first principles. *Phys. Rev. B* **93**, 1–5 (2016).
  124. Gu, X., Li, B. & Yang, R. Layer thickness-dependent phonon properties and thermal conductivity of MoS<sub>2</sub>. *J. Appl. Phys.* **119**, (2016).
  125. Liu, Z., Morales-Ferreiro, J. O. & Luo, T. First-principles study of thermoelectric properties of blue phosphorene. *Appl. Phys. Lett.* **113**, (2018).
  126. Akinwande, D. *et al.* A Review on Mechanics and Mechanical Properties of 2D Materials - Graphene and Beyond. *Extrem. Mech. Lett.* **13**, 42–77 (2016).
  127. Lindsay, L. & Broido, D. A. Three-phonon phase space and lattice thermal conductivity in semiconductors. *J. Phys. Condens. Matter* **20**, (2008).